ABSTRACT

ZHOU, HONGHUI. **Self-assembled Magnetic Nanostructures: Epitaxial Ni on TiN (001) Surface**. (Under the direction of Prof. Jagdish Narayan)

Systems that contain single domain magnetic particles have been receiving intensive attentions over recent years since they are possible candidates for applications in ultrahigh-density data storage and magnetoelectronic devices. The focus of this research is self-assembly growth of magnetic nickel nanostructures by domain matching epitaxy under Volmer-Weber (V-W) mode. The growth was conducted by pulsed laser deposition (PLD) technique using epitaxial titanium nitride film as the template, which was in turn grown on silicon (100) substrate. The structural characterization includes X-ray diffraction and both cross-sectional and plan-view transmission electron microscopy. The results showed that the nickel islands formed exhibit a self-assembled nature, i.e., a certain degree of uniformity in orientation, shape, and size. The orientation relationship observed is Ni {100} // TiN {100} // Si {100}, the so-called "cube-on-cube" relationship. The islands are faceted, forming truncated pyramids with walls of (111) planes and a flat top of (100) plane. The base of islands is rectangular with the two principal edges parallel to two orthogonal <011> directions. The size distribution is relatively narrow, comparable to that obtained from self-assembled islands grown under Stranski-Krastanov (S-K) mode. A certain degree of self-organization was also found in the island lateral distribution: island chains were observed along the directions close to <011>, which are also the edge directions. The island faceting could be explained by surface energy minimization. The interaction of the island edge induced strain field between neighboring islands is believed to be responsible for the size uniformity and the lateral ordering. Magnetic measurements were also conducted on these

crystallographically aligned nickel islands using superconducting quantum interference device (SQUID) magnetometer, and the results were compared with that obtained from the ensemble of randomly oriented nickel islands, which were grown on polycrystalline/amorphous Al_2O_3 matrix layer. It is found that both blocking temperature and coercivity of aligned nickel islands are significantly higher than that of the randomly oriented nickel islands. The enhancement in ferromagnetism is attributed to the increased collective effects resulting from the particle interactions in the ensemble of aligned islands, which are self-assembled and self-organized to some degree. Volmer-Weber growth of magnetic materials by domain matching epitaxy is a promising way to fabricate self-assembled magnetic nanostructures.

Self-assembled Magnetic Nanostructures:

Epitaxial Ni on TiN (001) Surface

by

Honghui Zhou

A dissertation submitted to the Graduate Faculty of

North Carolina State University

In partial fulfillment of the

Requirements for the degree of Doctor of Philosophy

In

Materials Science and Engineering

Raleigh, NC, Fall 2004

Approved by:

Prof. Jagdish Narayan	**Prof. Gerd Duscher**
Chair of Advisory Committee	
Prof. Carl C. Koch	**Prof. Robert M. Kolbas**

This dissertation is dedicated to

the memory of my father

Qikun Zhou

1935 – 1985

BIOGRAPHY

Honghui Zhou was born in Beijing, China, in 1966. She received her Bachelor of Engineering and Master of Engineering degree from the University of Science and Technology Beijing, China, in 1989 and 1992. She then worked as a research analyst in a scanning electron microscopy lab for six years before she made the decision to go to the United States of America to pursue a Ph. D. degree in the field of materials science. She first enrolled at University of Florida and studied there for one year before transferring to North Carolina State University to join Prof. Jagdish Narayan's group as a doctoral student in Department of Materials Science and Engineering in August of 2000.

ACKNOWLEDGEMENT

First, I would like to express my sincere gratitude to my supervisor, Prof. Jagdish Narayan, for providing me such an extraordinary research opportunity to work on this project, and for inspiring, guiding, and supporting me in the past four and half years. Without his supervision, I would not have been at the place where I am now.

I would like to sincerely thank Prof. Carl C. Koch, Prof. Robert Kolbas and Prof. Gerd Duscher for serving on the advisory committee and evaluating my thesis. Particularly, Prof. Gerd Duscher, who gave me lots of valuable advice and help.

Special thanks to Dr. Dhananjay Kumar for his collaboration in magnetic measurements, and also to Dr. Alexander V. Kvit, who had helped me with the transmission electron microscopy characterization during the early days of my thesis work and had given me TEM operation training.

I am also thankful to all people, who helped me in one way or another throughout this thesis work. They are Dr. Ashutosh Tiwari, Dr. Tapan Nath and all my fellow graduate students: Haiyan Wang, Chunming Jin, Abhishek Gupta, Jason Haverkamp, Thomas A. Rawdanowicz, Amit Chugh, Hugh Porter, Shivaraman Ramachandran, Vikram M. Bhosle, Punam Pant, Nathan G. Stoddard, and Wenjun Zhao. In particular, I would like to thank Chunming and Haiyan for their assistance in the lab work and for the valuable discussions I had with them concerning my research, and also Tom (Thomas), who, as the TEM lab manger after Dr. Alexander V. Kvit, has made great efforts to keep the electron microscopes operating efficiently.

I would also like to express my sincere thanks to Ms. Edna Deas, the student service assistant, who has helped me throughout these years on all sorts of administrative matters.

Finally, I would like to thank my mother and brother for their love, understanding, encouragement and support, which made this possible.

.

TABLE OF CONTENTS

LIST OF TABLES

LIST OF FIGURES

1 INTRODUCTION

The materials with reduced dimensions, including thin films (two-dimensional), fine wires (one-dimensional), and small particles (zero-dimensional), have attracted intensive research interests in past decades due to the novel and enhanced physical properties they exhibit over their bulk counterparts. The emergence of these novel properties is the direct result of the size confinement. For example, when the size of magnetic materials is reduced to be comparable to or smaller than certain characteristic length scales, e.g., domain wall width, new phenomenon appears, such as single domain state [1], and superparamagnetic relaxation [2-4]. When the separation between magnetic nanostructures is reduced below spin diffusion length, spin-polarized scattering/tunneling and giant magnetoresistivity (GMR), etc. can be observed [5]. Among those low-dimensional magnetic systems, small magnetic particles — the zero-dimensional magnetic systems — have been receiving special attentions over recent years due to the exciting application possibilities in data storage (e.g., ultrahigh density magnetic recording and magnetic random access memories (MRAMs)), and magnetic sensors in giant magnetoresistance (GMR) devices [6-7], etc.

Magnetic properties of a nanomagnetic material are closely related to the magnetic anisotropy of the material, which, for example, determines, to a large degree, the shape and the size of magnetic domains, coercive force and the shape of hysteresis loop [1]. Magnetic anisotropy can have several contributions, e.g., magnetocrystalline, shape, stress, surface, and therefore, depends not only on the size, shape and strain state of the particles, but also on their crystal structure and orientation. However, so far, most studies on magnetic nanostructures have been focused on the fabrication of randomly oriented particles and the

investigation of the dependence of magnetic properties on the particle size and separation. Very few works have been reported on the crystallographically aligned magnetic nanostructures [8-9].

The alignment of magnetic anisotropy is critical for the application of magnetic nanostructures in data storage and sensors. The dispersion of anisotropies will lead to variations in magnetic properties, such as switching field. According to the dynamic micromagnetic models developed by Ridley, *et al.* [6], the reversal mechanism of the arrays of magnetic nanostructures is very sensitive to the disorder of the anisotropies and a highly symmetric cooperative switching mechanism is observed in the case of aligned uniaxial anisotropy. The importance of aligning the anisotropies could be clearly manifested in the magnetic recording application.

Conventional thin film data storage medium is composed of small magnetic grains, which, ideally, are in single domain state and switch independently, i.e., no exchange coupling between the neighboring grains. Each bit of data, either 1 or 0 (the binary code used for digital data), is stored in a small patch of the film, which contains a number of magnetic grains [10]. The magnetization direction is parallel to the media surface, pointing either one way or the other (dictating either 1 or 0), and, therefore, is called longitudinal recording mode. In order to increase areal density, all the components, including the magnetic grains, need to be scaled to smaller dimensions. However, there are limits to the scaling. One limit comes from the demagnetization fields that approach a maximum in the vicinity of the transition between the two patches. If the patches are too small, they can be easily flipped by the magnetic field of their oppositely aligned neighbors, resulting in data loss. This problem

could be solved by employing a perpendicular recording mode, in which the magnetization direction is perpendicular to the media surface, and, therefore, the internal demagnetization field is reduced significantly near the transition [11-12]. The other limit is due to the superparamagnetic relaxation [2-4]. Below a certain critical size, the magnetization of the particles will become unstable against the thermal fluctuations, flipping between the easy axes and leading the data to be erased. Using discrete media, which contains isolated magnetic elements, has been considered to be currently the most promising approach to reach ultrahigh density storage device since it could delay the effect of the superparamagnetism limit till the areal density reaches as high as hundreds of gigabits per inch square. It has been demonstrated that a storage capability of 200 Gbits/in^2 was reached by using a discrete magnetic media, which contains magnetically isolated islands fabricated by focused-ion-beam lithography patterning [13]. In contrast to the conventional thin film media where one bit of information is stored in a tiny patch of the media containing a number of magnetic grains, the bit of information in discrete media scheme is written to one magnetic element, which is in single domain state, i.e., the element is entirely exchange coupled and able to switch as a unit [10,13-15].

The data storage requires predictable magnetization directions for these magnetic islands, in other words, the easy axes of the islands should be well controlled. In most cases, this is realized by making the shape of the islands elongated through patterning the polycrystalline magnetic film so that the shape anisotropy imparted will outweigh all the other anisotropy contributions and dominate the island magnetization behavior. However, for material with strong magnetocrystalline anisotropy, the shape anisotropy is not always able to outweigh magnetocrystalline anisotropy since as the island size gets smaller, there will be fewer crystal

grains, as a result, the magnetocrystalline anisotropy is less likely to be averaged out. If this happens, the easy directions of the islands, which are determined by the net magnetocrystalline anisotropy, will be randomly oriented. The dispersion of the easy axes will lead to variations in magnetic properties, such as switching field, and will cause the islands to relax into an unpredictable saturation remnant state after application and removal of the magnetic field [14,16-17]. In addition, the elongation of the island shape poses difficulties to device design and also contradicts the goal of achieving ultrahigh density, especially in the longitudinal recording mode. Patterning single crystalline instead of polycrystalline material will make it possible to control not only the particle shape, but also the crystallographic structure of the magnetic materials [14,17]. The resulting crystallographically aligned islands will have aligned easy axes if magnetocrystalline anisotropy dominates.

Discrete media was also called "patterned media" in the early days since lithography, a standard processing technique in semiconductor industry, has been employed to fabricate isolated magnetic islands. Electron beam lithography is the most commonly used type due to its high resolution. The fabrication of large numbers of magnetic nanostructures has been reported, such as 20 nm-sized Ni nanostructures by e-beam lithography combined with electroplating, and 20 nm-sized NiFe nanostructures by e-beam lithography combined with etching, etc. [18]. However, most lithographic processes could not be applied to single crystalline films since some processing steps, like the introduction of resists before completion of the film growth, would interrupt the epitaxial continuity of the film [19]. Besides, since the resolution of lithography is ultimately determined by the radiation wavelength, there is also a limit of the minimum feature size obtainable in this technique.

If the fabrication of nanostructures by lithography could be considered as a "top-down" approach since these nanostructures are "tailored" from infinitely large thin films, then there is also "bottom-up" approach under intense study, where nanostructures are built up with atoms, molecules and clusters. An extraordinary example of this is self-assembly growth, in which three dimensional (3D) islands are formed during heteroepitaxial growth of lattice mismatched materials. Obviously, self-assembly growth provides possible routes to fabricate oriented nanostructures without needing masking and patterning, and furthermore the size of the nanostructures obtained could even reach beyond the lithography limit. Therefore, self-assembly growth is attracting more and more attention from the researchers.

It is well known that for heteroepitaxial growth, there are three basic modes: (1) two-dimensional layer-by-layer growth (Frank-van der Merwe); (2) three-dimensional island growth (Volmer–Weber); and (3) two-dimensional (2D) followed by three-dimensional (3D) growth (layer-by-layer plus islands) (Stranski-Krastanov). Which mode the film growth takes depends on the surface energy, as well as the interfacial energy and the degree of lattice mismatch between the film and the substrate. So far, most self-assembled islands observed were grown under S-K mode. The condition for S-K growth is very demanding since it is the misfit strain accumulated in the system that finally induces the transition in the growth mode from 2D to 3D (the strain here is relieved first by forming islands rather than introducing dislocations) [20-24]. Therefore, most of the work on self-assembly has been conducted in a few semiconductor material systems, including Ge_xSi_{1-x} on Si, $In_xGa_{1-x}As$ on GaAs, InP on $In_xGa_{1-x}P$/GaAs and other III-V compounds**,** with the focus on the growth mechanism, optical properties and electronic structures [25-35].

It is worth pointing out here that the term "self-assembly" and "self-organization" is sometimes used interchangeably in the literature. In this study, "self-assembly" will be used when the deposited adatoms cluster into islands with similar size, shape, and orientation, while the term "self-organization" refers to the islands, which showed a certain degree of ordering in spatial distribution. The islands grown under S-K mode obviously can be called self-assembled because: they have the same orientation and similar shape due to the epitaxial growth and faceting; and also they have narrow size distribution due to the strain-induced kinetic limiting effect to the ripening [36-38]. However, these S-K mode grown islands are not necessarily well self-organized. There are only a few cases where apparent self-organization was observed [39-42]. The lateral ordering had been explained by the elastic interaction between neighboring islands through the substrate/wetting layer in a dense system of islands [38-41]. Approaches, which take advantages of heterogeneous nucleation on a preprocessed substrates, such as reconstructed [43-44], with dislocation networks [45-47], etc., haven been attempted to improve the lateral ordering.

Although most of self-assembly study so far has been limited to a few semiconductor systems, the growth has been explored to a large extent both experimentally and theoretically. On the other hand, there are only a few works on the metal or metallic alloy self-assembly growth [48-52]. The possible reason is that for metal growth, the system mismatch is not as easily controlled as that in semiconductor systems for the condition of S-K growth to be satisfied.

Compared with that of S-K growth, the growth condition for V-W epitaxy is less demanding, especially with the introduction of the concept of domain matching epitaxy (DME) since in

DME, the large misfit between the substrate and the film could be accommodated by interface dislocations [53-54]. The conventional concept of epitaxy actually only referred to the coherent epitaxy, therefore, it was once commonly accepted that the key consideration of epitaxial growth was the lattice mismatch between the film and substrate. The lattice mismatch should be small enough, e.g., a few percent, so that the film would grow pseudomorphically up to a "critical thickness" where it becomes energetically favorable for the film to contain dislocations. However, the epitaxial growth in systems with large lattice misfit, e.g., 22% in TiN/Si (100) system and 16.67% in ZnO/α-Al_2O_3 (0001) system, was observed [55-57]. Narayan proposed domain-matching epitaxy (DME) concept to explain this phenomenon [54]. According to Narayan, *et al.*, an array of dislocations is introduced in the first few monolayers of growth due to the lowered dislocation nucleation barrier by the large misfit. Therefore, the film is grown epitaxially with integral multiples of lattice planes matches those of the substrate. The size of the domain equals integral multiples of planar spacing with one dislocation in one domain. Although it is incoherent epitaxy, the epitaxial quality of the film grown by domain matching is considered to be better since the dislocations are confined within a few monolayers near the interface and their nature is dictated by the geometrical constraints of the growth process. In contrast, the dislocations in lattice matching epitaxy (LME) (with small lattice misfit) are generated at the film surface, which glide to the interface, forming dislocation loops. Therefore, with the introduction of DME concept, the system misfit is not a critical consideration anymore. The essential conditions for V-W epitaxy growth become only the symmetry compatibility between the structures of film and substrate, surface free energy of both film and substrate as well as the

interfacial free energy, which is mainly determined by the chemical bonding between the film and the substrate.

In V-W growth, the three-dimensional islands directly nucleate on the substrate surface, rather than on the wetting layer as in S-K growth. Therefore, if terminated at the early stage, it is also possible to have self-assembled islands. However, this growth mode has not been seriously considered as a method for obtaining self-assembled islands, which is probably due to the non-uniform size distribution of the islands expected as a result of Ostwald Ripening [58-60]. The reports on the size distribution are not consistent and both broad [61-62] and narrow size distribution [48,63] have been reported, which probably resulted from the difference in the growth conditions. Even if Ostwald Ripening is thermodynamically favorable, it could still be kinetically limited by factors that commonly exist in V-W epitaxy growth by deposition, such as the induced strain field, which could affect diffusion [65], or supersaturation, which determines both nucleation and growth rate, etc. Therefore, a detailed study of the island growth under V-W mode is necessary to explore this new, more widely applicable approach to the nanostructure fabrication, especially for the applications where defect (dislocation)-free interface is not that critical for the device performance.

In this work, the epitaxial growth of nickel on titanium nitride (100) surface is investigated. Based on the surface free energies of nickel and titanium nitride, this growth was expected to be three-dimensional island growth following V-W mode by domain matching epitaxy. Titanium nitride was chosen as the template because it can be grown epitaxially at relatively low temperatures on silicon substrates through domain matching epitaxy (DME) [55-56]. Additionally, it is of significant importance to integrate magnetic nanostructures with silicon,

the base material of the semiconductor industry. Nickel was chosen as the magnetic material based on the fact that it remains fcc (face-centered cubic) throughout the whole temperature range and, therefore, its epitaxial growth is more controllable [1]. In comparison, cobalt experiences a structure change around 430 ˚C from hcp (hexagonal close-packed) to fcc. The goal of our investigation is the development of a method to produce self-assembled crystallographically aligned metal nanostructures in a controlled way for a variety of applications ranging from ultrahigh density data storage to magnetoelectronic devices.

This thesis includes eight chapters. In Chapter 2 some related background knowledge is summarized, including magnetism of nanostructured materials, pulsed laser deposition technique, and nucleation and growth of thin films. Chapter 3 covers the experimental methods, including growth, structural and magnetic characterizations. Results and discussion parts are presented from Chapter 4 through 7. Chapter 4 covers the cross-sectional TEM study of nickel epitaxial growth on titanium nitride (001) surface, such as growth mode, epitaxial orientation, island shape and faceting. The results of island size distribution and lateral ordering were mainly extracted from plan-view TEM study, which is presented in Chapter 5. Chapter 6 shows the structural information of multi-layered samples. For stronger signal, magnetic measurements were conducted on multi-layered samples, which contains layers of nickel islands separated by either epitaxial titanium nitride or polycrystalline/amorphous aluminum oxide layers. The introduction of aluminum oxide matrix is to grow crystallographically randomly oriented nickel islands, whose magnetic behavior could serve as the reference for that of nickel islands grown in epitaxial titanium nitride matrix, which are expected to be crystallographically aligned. The results of magnetic characterization of the two systems are presented in Chapter 7 and Chapter 8 summarizes the

conclusions. Part of this work has been published in several journal and conference papers [66-70].

References

1. B. D. Cullity, *Introduction to Magnetic Materials*, Addison-Wesley, Reading, Masschusetts, (1972)
2. L. Néel, Ann. Geophys. (C.N.R.S) **5**, 99 (1949)
3. R. C. Stoner, and E. P. Wohlfarth, Philos. Trans. R. Soc. London, Ser. A **240**, 599 (1948)
4. C. P. Bean, and J. D. Livingstone, Appl. Phys. **30**, 120S (1959)
5. M. N. Baibich, J. M. Broto, A. Fert, F. Nguyen van Dau, F. Petroff, P. Etienne, G. Greuzet, A. Friederich, and J. Chazeles, Phys. Rev. Lett., **61**, 2472 (1991)
6. P. H. W. Ridley, G. W. Roberts, and R. W. Chantrell, J. Appl. Phys., **92** 1069 (2002)
7. S.W. Yuan, and H.N. Bertram, J. Appl. Phys. **75**, 6385(1994)
8. Bo Bian and Yoshihiko Hirotsu, Jpn. J. Appl. Phys. **36,** L1232 (1997)
9. B. Bian, Y. Hirotsu, and A. Makino, NanoStructured Materials, **8**, 1057 (1997)
10. R. L. White, R. M. H. New, and R. F. W. Pease, IEEE Trans. Magn. **33**, 990 (1997)
11. Jack H. Judy, J. Magn. Magn. Mater. **235**, 235(2001)
12. P. Singer, Semiconductor International, Vol. **25**, Iss.10, 50 (2002)
13. M. Albrecht, C. T. Rettner, A. Moser, M. E. Best, and B. D. Terris, Appl. Phy. Lett. **81**, 2875 (2002)
14. S. Ganesan, C. M. Park, K. Hattori, H. C. Park, R. L. White, H. Koo, and R. D. Gomez, IEEE Trans. Magn. **36**, 2987 (2000)
15. M. Albrecht, S. Ganesan, C. T. Rettner, A. Moser, M. E. Best, R. L. White, and B. D. Terris, IEEE Trans. Magn. **39**, 2323 (2003)
16. R. M. H. New, R. F. W. Pease, and R. L. White, IEEE Trans. Magn. **31**, 3805 (1995)
17. R. M. H. New, R. F. W. Pease, and R. L. J. White, Appl. Phys., **79**, 5851 (1996)
18. J. I. Martín, J. Nogués, Kai Liu, J. L. Vicent, and Ivan K. Schuller, J. Magn. Magn. Mater., **256**, 449 (2003), and references therein

19. R. M. H. New, R. F. W. Pease, and R. L. J. White, Vac. Sci Technol. B **12**, 3196 (1994)

20. Serge Luryi, and Ephraim Suhir, Appl. Letts., **49**, 140 (1986)

21. D. J. Eaglesham, and M. Cerullo, Phys. Rev. Letts., **64**, 1943 (1990)

22. J. Tersoff, and F. K. LeGoues, Phys. Rev. Letts., **72**, 3570 (1994)

23. S. Christiansen, M. Albrecht, H. P. Strunk, P. O. Hansson, and E. Bauser, Appl. Phys. Letts., **66**, 574 (1995)

24. L. J. Gray, M. F. Chrisholm, and Theodore Kaplan, Appl. Letts., **66**, 1924 (1995)

25. Y. –W. Mo, D. E. Savage, B. S. Swartzentruber, and M. G. Lagally, Phys. Rev. Letts. **65**, 1020 (1990).

26. D. J. Eaglesham, F. C. Unterwald, and D. C. Jacobson, Phys. Rev. Letts. **70**, 966 (1993).

27. M. Goryll, L. Vescan, K. Schmidt, S. Mesters, H. Lüth, and K. Szot, Appl. Phys. Lett. **71**, 410 (1997).

28. Vinh Le Thanh, P. Boucaud, D. Débarre, Y. Zheng, D. Bouchier, and J-M Lourtioz, Phys. Rev. B. **58**, 13115 (1998).

29. A. Madhukar, Q. Xie, P. Chen, and A. Konkar, Appl. Phys. Letts. **64**, 2727 (1994).

30. D. Leonard, K. Pond, and P. M. Petroff, Phys. Rev. B. **50**, 11687 (1994).

31. D. Leonard, M. Krishnamurthy, S. Fafard, J. L. Merz, and P. M. Petroff, J. Vac. Sci. Technol. B. **12**, 1063 (1994).

32. D. Leonard, M. Krishnamurthy, C. M. Reaves, S. P. Denbaars, and P. M. Petroff, Appl. Phys. Letts. **63**, 3203 (1993).

33. Pawel Hawrylak and Arkadiusz Wojs, Semicond. Sci. Technol. **11**, 1516 (1996).

34. B V Volovik, A R Kovsh, W Passenberg, H Kuenzel, N Grote, N A Cherkashin, Yu G Musikhin, N N Ledentsov, D Bimberg, and V M Ustinov, Semicond. Sci. Technol. **16**, 186 (2001).

35. A E Zhukov, V M Ustinov, A R Kovsh, A Yu Egorov, N A Maleev, N N Ledentsov, A F Tsatsul'nikov, M V Maximov, Yu G Musikhin, N A Bert, P S Kop'ev, D Bimberg and Zh l Alferov, Semicond, Sci. Technol. **14**, 575 (1999).

36. N. P. Kobayashi, T.R. Ramachandran, Chen, P., and Madhukar, A., Appl. Phys. Lett., **68**, 3299 (1996)

37. Y. Chen, and J. Washburn, Phys. Rev. Lett., **77**, 4046 (1996)

38. Albert-László Barabási, Appl. Phys. Lett., **70**, 2565 (1997)

39. A. Vitaliy Shchukin, and Dieter Bimberg, Rev. Modern Physics, **71**, 1125 (1999), and the references therein.

40. K. Zhang, Ch. Heyn, W. Hansen, Th. Schmidt, and J. Falta, Appl. Phys. Lett., **76**, 2229 (2000)

41. M. Meixner, E. Schöll, M. Schmidbauer, H. Raidt, and R. Köhler, Phys. Rev. B **64**, 245307 (2001)

42. M. Hanke, H. Raidt, R. Köhler, and H. Wawra, Appl. Phys. Lett. **83**, 4927 (2003).

43. A.Voigtländer, G. Meyer, and N.M. Amer, Phys. Rev. B, **44**, 10354 (1991)

44. H. Takeshita *et al.*., Appl. Phys. Lett. **68**, 3040 (1996)

45. D.D. Chambliss, R.J. Wilson, and S. Chiang, Phys. Rev. Lett., **66**, 1721 (1991)

46. H. Brune, M. Giovannini, K. Bromann, and K. Kern, Nature (London) **394**, 451 (1998);

47. K. Bromann, M. Giovannini, H. Brune, and K. Kern, Eur. Phys. J. D **9**, 25 (1999)

48. Chengtao Yu, Dongqi Li, J. Pearson, and S. D. Bader, Appl. Phys. Lett. **78**, 1228 (2001).

49. A.Bonanni, H. Seyringer, H. Sitter, D. Stifter, and K. Hingerl, Appl. Phys. Lett. **74**, 3732 (1999).

50. O. Fruchart, M. Klaua, J. Barthel, and J. Kirschner, Phys. Rev. Lett. **83**, 2769 (1999)

51. S. L. Silva, C. R. Jenkins, S. M. York, and F. M. Leibsle, Appl. Phys. Lett. **76**, 1128 (2000).

52. Feng Liu, Phys. Rev. Lett. **89**, 246105 (2002)

53. J. Narayan, and S. Oktyabrsky, J. Appl. Phys., **92**, 7122 (2002)

54. J. Narayan, and B. C. Larson, J. Appl. Phys., **93**, 278 (2003)

55. J. Narayan, P. Tiwari, X. Chen, R. Chowdhury, and T. Zheleva, Appl. Phys. Lett., **61**, 1290 (1992)

56. J. Narayan, U.S. Patent No. 5,406, 123 (1995)

57. J. Narayan, K. Dovidenko, A. K. Sharma, and S. Oktyabrsky, J. Appl. Phys., **84**, 2597 (1998)

58. M. Iwamatsu, and Y., J Okabe, Appl. Phys. **86**, 5541 (1999)

59. R. D. Vengrenovich, Yu. V. Gudyma, and S. V. Yarema, Semiconducors, **35**, 1378 (2001)

60. A. Howard, C. E. J. Mitchell, and R. G. Egdell, Sur Sci, **515**, L504 (2002)

61. M.C. Harris Liao, Y.H. Chang, Y. F. Chen, J. W. Hsu, J. M. Lin, and W.C. Chou, Appl. Phys. Lett., **70**, 2256 (1997)

62. R. Leon, C. Lobo, T. P. Chin, J. M. Woodall, S. Farard, S. Ruvimov, Z. Liliental-Weber, M. A., Stevens Kalceff, Appl. Phys. Lett. **72**, 1356 (1998)

63. S.O. Ferreira, B. R. A. Neves, R. Magalhães-Paniago, A. Malachias, P.H.O. Pappl, A.Y. Ueta, E. Abramof, and M. S. Andrade, J. Crystal Growth, **231,** 121 (2001)

64. Chengtao Yu, Dongqi Li, J. Pearson, and S. D. Bader, Appl. Phys. Lett. **78**, 1228 (2001).

65. M. Schroeder, and D. E. Wolf, Surf. Sci., **375**, 129 (1997)

66. H. Zhou, D. Kumar, A. Kvit, A. Tiwari, and J. Narayan, J. Appl. Phys. **94**, 4841 (2003)

67. H. Zhou, A. Kvit, D. Kumar, and J. Narayan, MRS Proceedings Fall (2001)

68. H. Zhou, D. Kumar, A. Kvit, A. Tiwari, and J. Narayan, MRS Proceedings, DD5 19.1 Fall, 2002

69. D. Kumar, H. Zhou, T. K. Nath, A. Kvit, and J. Narayan, Appl. Phys. Lett., **79**, 2817 (2001)

70. D. Kumar, H. Zhou, T. K. Nath, A. Kvit, and J. Narayan, J. Mater. Res. , **17**, 738 (2002)

2 RELATED BACKGROUND KNOWLEDGE

2.1 MAGNETISM OF NANOSTRUCTURED MATERIALS

This part covers the special phenomena/properties in nanostructured magnetic materials.

2.1.1 Single-domain State

As well known, the multi-domain state in ferromagnetic materials is the result of a total energy minimization [1]. The competing energy terms involved are exchange energy, which favors a parallel aligning of all the magnetic moments, and magnetostatic energy, which favors an antiparallel aligning [1]. However, there exists a critical size, below which this multi-domain configuration becomes energetically unfavorable and the material could only acquire single domain even in the zero magnetic field [1]. Inside the single domain structure, the atomic magnetic moments are coupled via exchange interactions to form a large net cluster moment [1].

For most materials the critical single domain size is on the order of a few hundred Å. It not only depends on the material, through exchange constant, magnetic moment per unit volume, and intrinsic anisotropy [1], but also on the particle shape and the aspect ratio [2]. Usually, materials with higher exchange constant/anisotropy tend to have larger critical single domain size, whereas materials with lower magnetic moment tend to have smaller critical single domain size. The main effects of the shape and aspect ratio on the magnetization state of single particles are sketched in Fig. 2.1 (from Ref. [2]). Compared to the square or

rectangular nanostructures, the circular or ellipsoidal nanostructures have larger critical single domain size.

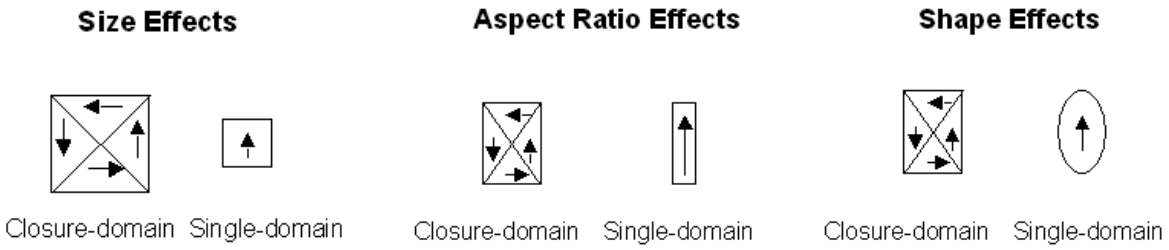

Figure 2-1 Schematic illustration of some typical effectss (size, aspect ratio and shape) on the magnetic configuration at H=0 (for the same magnetic materials at constant temperature) (Ref. [2])

Single domain configuration causes the nanostructures to exhibit higher magnetic coercivity than that of the bulk materials. This effect was explained by the fact that in single domain structures, the magnetization reversal could only take place by rotation of the magnetization vector, either coherent or incoherent, and this rotation could be very difficult since it is against the strong anisotropy forces (magnetocrystalline, shape, stress, etc, which will be discussed in section 2.1.3). The anisotropy energy barrier for particles with uniaxial anisotropy is generally written as [1]:

$$E(\theta) = -KV\cos^2\theta \tag{2.1}$$

where K is the magnetic anisotropy constant, V is the volume of the particle and θ is the angle between the magnetization vector and the magnetization easy direction.

Fig. 2.2 **(**from Ref. [3]) is a schematic illustration for the magnetic energy of an ellipsoidal particle in the absence of external magnetic fields, which summarizes the key concepts underlying both the Stoner-Wohlfarth [4] and Néel-Brown [5-6] models of the magnetic dynamics of small magnetic particles. Ellipsoidal particles sketched here are assumed to have two stable states (have uniaxial anisotropy). Stoner and Wohlfarth [4] proposed that as the external magnetic filed is varied, one of the states will become unstable with respect to the other and the total spin of the particles may flip.

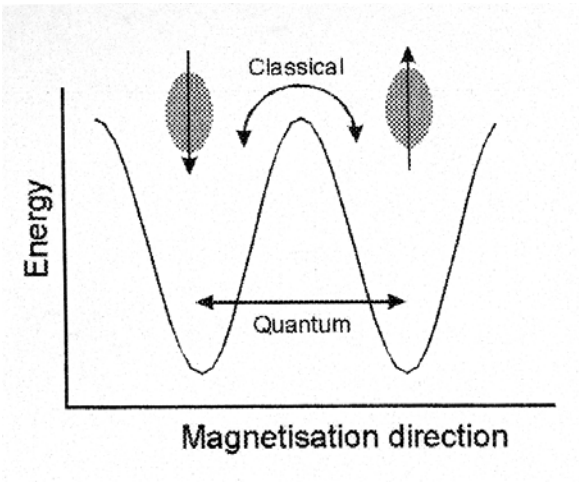

Figure 2-2 A simple schematic illustration of the energy of a magnetic nanoparticle versus the magnetization direction. There are two equivalent energy minima related to the "spin-up" and "spin-down" states of the particle. The spin state can flip between these two minima either via a classical, barrier-surmounting path or via quantum mechanical tunneling (Ref. [3]).

Assuming coherent rotation, if the particles anisotropy is uniaxial with the easy axes aligned with the field, then the coercivity due to magnetocrystalline, shape and stress anisotropy is given by [1]

(magnetocrystalline) $$H = h(\frac{2K_1}{M_S}) \quad (2.2)$$

(SHAPE) $$H = h(N_a - N_C)M_S \quad (2.3)$$

(stress) $$H = h(\frac{3\lambda_{si}\sigma}{M_S}) \quad (2.4)$$

where K_1 is the crystalline anisotropy constant; N_a and N_c are the demagnetizing coefficients parallel to *a* and *c* axes, respectively; λ_{si} is the saturation magnetostriction (assumed isotropic) and σ is the stress.

The coercivity of particles has strong size dependence, as shown in Fig. 2.3 (adapted from Ref. [1]). As the size is decreased in multi-domain regime, the coercivity increases and reaches the maximum when entering the single domain regime. After that the coercivity decreases with the size due to the lowered anisotropy energy barrier for magnetic moment rotation, which is proportional to the particle volume. When the size further decreases, the superparamagnetism will set in and the particles lose hysteresis behavior, therefore, no coercivity is observed. The superparamagnetism will be discussed in section 2.1.2.

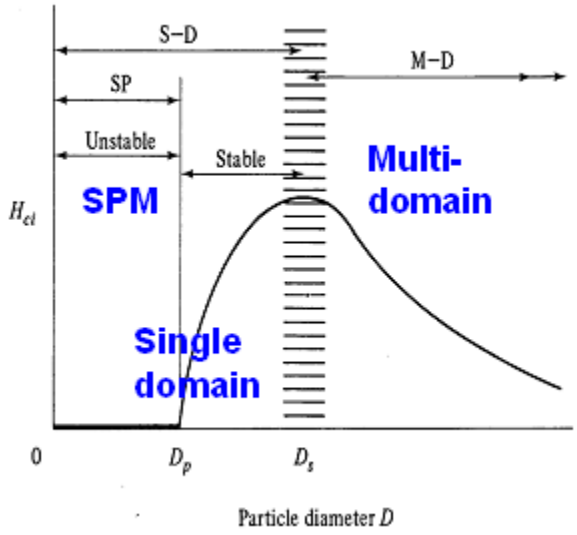

Figure 2-3 A schematic diagram of variation of intrinsic coercivity H_c with particle diameter D (Ref. [1]).

2.1.2 Superparamagnetism

The superparamagnetic phenomenon was predicted by Néel early in 1949 [5]. He pointed out that under a certain temperature as the single domain particle size decreases, the anisotropy energy barrier (KV, with K the anisotropy constant and V the particle volume) for the rotation of magnetic vector of the particle decreases and finally could be overcome by the thermal energy (k_BT, with k_B the Boltzmann constant and T the temperature). As a result, the magnetic vector fluctuates rather than being fixed (blocked). This is just like the behavior of a normal paramagnetic material with the difference that the single domain particle contains a large number of atoms, and thus posses a much higher magnetic moment (e. g. 5590 atoms, and therefore 1200 μB for a Fe particle of diameter of 5 nm). That is the reason that Bean, *et*

al. coined the term superparamagnetism to describe this behavior [7]. Certainly, for particles with a certain size, the anisotropy energy barrier could also be overcome by the thermal energy when the temperature increases. The temperature where the superparamagnetism sets in is called blocking temperature. The thermal activated reversal frequency is given by the Arrenius law:

$$\nu = \nu_0 \exp(-KV / k_B T) \tag{2.5-a}$$

where ν_o is the attempt frequency, which is normally taken to be $\sim 10^9$ s^{-1}, and KV is the anisotropy energy barrier separating the two spin states. Equivalently, the relaxation time τ, a statistical time needed to finish a thermal activated reversal, is given by:

$$\tau = \tau_0 \exp(KV / k_B T) \tag{2.5-b}$$

Superparamagnetism could be observed by using instruments. Therefore, the characteristic measurement time inevitably plays a critical role and the term such as "blocking temperature" and "critical size" is meaningful only in the context of characteristic measurement time. For example, the blocking temperature measured is directly related to the characteristic measurement time τ_i by [8]

$$T_{Bi} = \frac{KV}{k_B[\ln(\tau_i / \tau_0)]} \tag{2.6}$$

when taking τ_i=100 s, which is commonly used in measurements, it gives the usual criterion of blocking temperature T_B = KV/25 k_B, while when taking τ_i=1 hour, it gives T_B = KV/30k_B.

2.1.3 Anisotropy of Small Magnetic Particles

As mentioned in section 2.1.1, the spins are exchange coupled inside a single domain particle. The total magnetic energy has a dependence on this spin direction. The directions with the lowest energy are defined as "easy directions" and they are separated by a "anisotropy energy barrier", i.e., the energy barrier needs to be overcome for a magnetization vector to rotate. Therefore, anisotropy is one of the most important properties of small magnetic particles because it determines the magnetic reversal process. It has been found that the value of the anisotropy energy constant (energy per unit volume) in microcrystals obtained by using Mösbauer spectroscopy was considerably greater than those of large crystals [9]. This is probably because for small magnetic particles the contributions to the total anisotropy might come from lots of sources, such as magnetocrystalline, shape, surface/interface, stress, and interaction, etc. The rest of this section will briefly discuss these anisotropy sources.

1. Magnetocrystalline anisotropy

Magnetocrystalline anisotropy is an intrinsic anisotropy, which is crystal structure-related. It is mainly a result of the spin-orbit coupling. When an external field tries to reorient the spin of an electron, the orbit of that electron also tends to be reoriented due to this coupling. However, the orbit is already strongly coupled to the lattice by orbit-lattice coupling. Therefore, to rotate the spin system of a domain away from the easy direction, energy is required to overcome this spin-orbit coupling.

The easy/hard directions determined by magnetocrystalline anisotropy are along some specific crystallographic directions, which depend only on the type of crystal structure. For cubic crystals and hexagonal crystals the magnetocrystalline energy per unit volume can be written as:

$$E^{cubic}{}_{xtal} = K_0 + K_1(\alpha_1{}^2\alpha_2{}^2 + \alpha_2{}^2\alpha_3{}^2 + \alpha_3{}^2\alpha_1{}^2) + (\alpha_1{}^2\alpha_2{}^2\alpha_3{}^2) + \ldots \quad (2.7)$$

$$E^{hex}{}_{xtal} = K_0' + K_1'\sin^2\theta + K_2'\sin^4\theta + \ldots \quad (2.8)$$

where K_i and K_i's are energy constants, which depend on the material characteristics and the temperature; α_i is the cosine of the angle between the spin direction and the three cubic crystal axes and θ is the angle between the spin direction and the *c* axis of the hexagonal crystal.

For example, bulk iron has <100> and <111> as easy and hard direction, respectively. Whereas bulk nickel and all cubic ferrites, except those containing large amount of cobalt, are the opposite: <111> is the easy direction and the <100> is the hard direction. The magnetocrystalline anisotropy strongly depends on the temperature. Mostly the anisotropy decreases as the temperature increases and becomes essentially zero even before the Curie temperature is reached. Cobalt, on the other side, has a hexagonal structure, the easy direction is along the *c* axis up to 245 ºC, and becomes inclined to the basal plane for temperature between 245 ºC – 325 ºC and lies in the basal plane for temperatures higher than 325 ºC [1].

2. Shape anisotropy

Shape anisotropy is of special importance for small magnetic particles. It arises when the shape of the materials deviates from the ideal sphere. Shape anisotropy is mainly due to the magnetic dipolar interactions [10]. Generally speaking, the easy axis always lies along the long axis rather than the short axis because the demagnetization field along a short axis is stronger than that along a long axis [1]. Therefore, the rectangular or elliptical particles tend to have easy axis along the long axis of the elements [2] and the magnetization of an oblate spheroid (disk) is difficult along the short axis and equally easy along any axis normal to it in the plane of the disk [1]. The strength of shape anisotropy depends on the axial ratio as well as the extent of magnetization [1].

The shape anisotropy energy per unit volume of ellipsoid particle could be written as [1, 9]:

$$E^{ellipsoid}{}_{shape} = \frac{1}{2} M_S{}^2 (N_a - N_c) \sin^2 \theta \tag{2.9}$$

N_a and N_c are the demagnetizing coefficients along *a* (semi minor axis) and *c* (semi major axis), respectively, and θ is the angle between the spin direction and the easy axis, which is *c* if $c > a$.

Shape anisotropy could become dominant when the shape axial ratio is big enough, and the material has weak magnetocrystalline anisotropy, or the magnetocrystalline anisotropy is averaged out in big polycrystalline particles with large number of grains.

3. Stress anisotropy

Stress anisotropy comes from the inverse effect of the magnetostriction or magnetomechanical effect. The magnetization behavior of the materials could be affected by the applied stress. For example, the tensile stress reduces the magnetization of nickel at low field (negative magnetostriction). In other words, stress alone could create an easy axis of magnetization, as the result of the magnetoelastic energy minimization. The magnetoelastic energy per unit volume could be written as [1, 9]:

$$E^{isotropic}{}_{elastic} = -\frac{3}{2}\lambda\sigma\cos^2\theta \tag{2.10}$$

Where λ is the magnetostriction constants, σ is the stress ("+" for tensile and "-" for compressive), and θ is the angle between the spin and stress directions. Whether the stress axis is the easy or the hard axis depends on the sign of λσ. The stress axis is an easy axis if this quantity is positive and the stress axis is a hard axis (the plane normal to the stress axis becomes an easy plane of magnetization) if the quantity is negative. In nickel for example, this quantity is negative under tension since it has negative magnetostriction, and, therefore the stress axis is the hard axis [1]. The spin-orbit interaction in conjunction with the overlapping of the wave functions between neighboring atoms, is responsible for the stress anisotropy [10]. For particles imbedded in a matrix (as it is the case in this study), the stress anisotropy must be considered.

4. Surface/interface anisotropy

Surface/interface anisotropy becomes pronounced in particles since their surface/volume ratio is the highest among low-dimensional magnetic systems. The source of surface/interface anisotropy is the same as that of magnetocrystalline anisotropy — spin-orbit coupling. The distinction between surface and interface is based on whether vacuum or another material present at the boundary of a material. The surface anisotropy is due to the lowered symmetry at the surface and interface anisotropy basically originates from the lack of translational symmetry at the interface. The resulting reduction in coordination numbers of the surface/interface atoms introduces frustration and spin disorder [2]. The surface/interface anisotropy leads the easy axis parallel to the surface/interface normal. The well-known perpendicular magnetic anisotropy (PMA) phenomenon is a typical example of surface/anisotropy.

5. Exchange anisotropy

Exchange anisotropy arises from an exchange interaction at the interface between two magnetic systems, normally a ferromagnet and an antiferromagnet. The common case in particle systems, where exchange anisotropy is observed, is the ferromagnetic particles with the antiferromagnetic oxide shell, e.g. the first experimental observation of exchange anisotropy was in a system of cobalt particle with oxidized surface [11]. The direct exchange coupling between ferromagnets and antiferromagnets causes the uncompensated spins at the surface of antiferromagnets. The generation of these uncompensated spins is the result of a field cooling process that steps across the blocking temperature of the ferromagnet and the Néel temperature of the antiferromagnet [1,12]. The main feature of exchange anisotropy is

the occurrence of a displacement in the hysteresis loop of coupled system. The amount of the shift is used to describe the exchange coupling and called exchange field H_{ex}, which is determined by the number and direction of the uncompensated spins [12].

6. Interaction anisotropy

All the anisotropies mentioned earlier are for isolated particles. As a matter of fact, it was found that when the neighboring particles are close enough, their moments would interact (dipolar interaction) leading to an additional anisotropy. The easy axis is determined by the relative positions of the two coupled systems [9]. This interaction is expected to play a role in the properties of self-assembled and self-organized nanostructured magnetic materials such as produced in this study.

References

1. B. D. Cullity, *Introduction to Magnetic Materials*, Addison-Wesley, Readings, Massachusette (1972)

2. J. I. Martin, J. Nogues, Kai Liu, J. L. Vicent, Ivan K. Schuller, J. Magn. Magn. Mater., **256**, 449 (2003)

3. S. Gider, D. D. Awschalom T. Doughlas, S. Mann, and M. Chaparala, Science, **268**, 77 (1995)

4. R. C. Stoner, and E. P. Wohlfarth, Philos. Trans. R. Soc. London, Ser. A **240**, 599 (1948)

5. L. Néel, Ann. Geophys. (C.N.R.S) **5**, 99 (1949)

6. W. F. Brown, Phys. Rev., **130**, 1677 (1963)

7. B. P. Bean, and J. D. Livingstone, Appl.Phys. **30**, 120S (1959)

8. B. L. Chien, *Nano*STRUCTURED MATERIALS, **1**, PP 179-184 (1992)

9. S. Mørup, J. A. Dumesic, and H. Topsøe, in *Applications of Mössbauer Spectroscopy*, edited by R. L. Cohen, Academic, New York (1980), Vol. **2**, Chap. 1

10. M T Johnson, P J H Bloemen, F J A den Broeder and J J de Vries, Rep. Prog. Phys. **59**, 1409 (1996)

11. W. P. Meiklejohn and C. P. Bean, Phys. Rev. **102**, 1413 (1956)

12. P. A. Grünberg, Sensors and Actuators, A **91**, 153 (2001)

2.2 PULSED LASER DEPOSITION TECHNIQUE

2.2.1 General Remarks

Since the pulsed laser in the nanosecond (ns) regime became available in late 1970's and, especially, the successful growth of high T_c superconducting films in 1987 [1,2], pulsed laser deposition (PLD) has become more and more popular in research laboratories serving as an effective technique to grow a wide variety of novel thin film structures [3,4], such as artificially layered superconducting materials [5], epitaxial superconducting films [6], and diamond-like carbon (DLC) films [7-9], etc. The feature that makes PLD so distinguished from other deposition techniques is the use of pulsed laser beam to heat and vaporize the target material.

In terms of experimental set-up, this technique is quite simple, which, to a large degree, leads to the low start-up cost of the technique. A basic PLD system includes three components: a high-power laser, a vacuum chamber housing both the target and the substrate holder, and a set of optical elements, including lenses, apertures, mirrors, etc., which is positioned between the first two. During the deposition, the laser beam is directed into the vacuum chamber and focused on the target surface by the set of optical components. If the laser fluence (the energy density deposited on the target surface) reaches a threshold value [10], significant material removal of the target material would occur in the form of a luminous plasma plume, which is usually oriented along the target surface normal, or skewed a few degrees toward the incoming laser beam in some cases for the non-normal incidence [3]. The plume consists of a mixture of energetic species including atoms, molecules, electrons, ions, and sometimes,

micron-sized particulates and molten globules. These species will then recondense on the substrate surface forming the thin film. The threshold ablation fluence depends not only on the laser parameters (wavelength and the pulse duration, etc.), but also on the target material properties, such as optical absorption, thermal conducting, and the target surface morphologies as well [10].

In general, the useful range of laser wavelength for thin film growth by PLD lies between 200 nm and 400 nm, a spectral region where most of the materials exhibit strong absorption. Excimer lasers and Nd^{3+}: YAG lasers are the two most commonly used lasers in previous PLD works. Nd^{3+}: YAG lasers are solid-state laser systems. Although the fundamental laser emission of Nd^{3+}: YAG occurs at 1064 nm, the out-put radiation frequency could be brought to the desired region by using a nonlinear crystal and the repetition rates of high power Q-switch Nd^{3+}: YAG laser could be as high as 30 Hz. In contrast, excimer lasers are gas laser systems and they can emit radiation directly in the UV range with the repetition rate up to several hundred hertz and the energies over 500 mJ/pulse. The radiation wavelength is determined by the gas used, varying from 157 nm for F_2 to 351 nm for XeF. KrF laser, which emits laser of wavelength at 248 nm (photon energy of 5 eV), is the most popular choice among the PLD community since being the highest gain system for electrically discharged pumped excimer lasers, KrF laser is able to deliver pulses with much higher energy than other excimer lasers [11].

2.2.2 Strength and Weakness

The use of laser as vaporization source renders PLD technique key advantages not available with other systems.

From a viewpoint of deposition technique, unlike ions or electrons, laser beam is much easier to transfer and manipulate. Also the decoupling of the heating source (laser) from the vacuum system makes it relatively easy for the system to adapt different operation modes and incorporate new features. In addition, the interaction between the laser and the gas species is relatively weak, and as a result, the dynamic range of the deposition pressure could be relatively high, which means less stringent requirements for the vacuum system. Furthermore, the spatial confinement of the laser-target interaction and the subsequent confined evaporant in PLD makes the process relatively clean, and therefore the thin films deposited free of contamination compared to, say, sputtering techniques, where the plasma of the sputtering process tends to contact with various surfaces inside the chamber. Finally, the pulsed nature of PLD may allow the film thickness (the amount of material to be deposited) to be precisely controlled. Therefore, it is quite straightforward using PLD to prepare composite films with different layers made from materials with different dielectric properties, simply by positioning the desired target under the laser beam ablating for appropriate duration.

Using laser as heating source also makes PLD an extremely versatile technique in terms of the material applicability. On the one hand, since at a wavelength of 250 nm and below, virtually all material absorb the laser beam either via linear or nonlinear processes, almost all materials, independent of its dielectric properties, could be deposited by PLD as long as an appropriate laser is available [12]. On the other hand, due to the nonequilibrium nature of the evaporation, the stoichiometry of the target could be faithfully reproduced in the film under optimum conditions, which makes PLD a superior choice for depositing multicomponent films. As a matter of fact, the list of the thin films that have been prepared by PLD includes

materials ranging from insulators to superconductors; and from pure elements to compounds with up to six elements [13,14].

From a pointview of film growth, there are two important aspects that distinguish PLD from other deposition techniques. One is the ultrahigh instantaneous deposition rate resulting from the pulsed nature of the evaporation. The other is the high kinetic energy of the incident species. These two factors have significant influence on the thin film growth process, which will be discussed in a separate section (Section 2.3.2).

However, there are two major drawbacks in PLD technique [3]: the lack of film thickness uniformity in large area and the particulate deposition. The former one is due to the forward peaking nature of the plume, i.e., the plasma elongates preferentially perpendicular to the target surface [6, 10, 15], and the latter one originates from the explosive nature of laser-target interaction [16-18].

The thickness spatial variation of films deposited by PLD has been found to be $\cos^n\theta$ with θ being the angle between the radial vector and the normal to the target surface and n varying around 8-12 depending on the laser parameters and irradiated spot size, etc. This is significantly different from $\cos\theta$, the thickness variation of films deposited by a conventional thermal process [6, 10, 19, 20]. Singh and Narayan developed a theoretical model to simulate the pulsed laser evaporation process and found that the forward-directed nature was due to the anisotropic expansion velocities of the plume, which are driven by the density gradients in the plasma, and a higher-energy density results in a more forward-directed nature of the laser output [6, 10]. This characteristic makes the large scale-up a challenging task.

Engineering solutions like rastering the laser on the substrate using rotation and translation have been proposed [21].

The particulates production is an intrinsic problem, in which several mechanisms are involved, such as subsurface boiling, expulsion of the liquid layer by the shock wave recoil pressure, and exfoliation [3, 22, 23]. The dimensions and the number density of particles are found to be related to deposition parameters including, pulse energy density, optical absorption coefficient, and the thermophysical properties of the target [23]. Subsurface superheating model suggested by Singh *et al.* [16] predicts that the particle density in PLD films can be considerably reduced by increasing the absorption coefficient and/or the thermal conductivity of the target material, and also by increasing the cohesion of the target grains. These predictions were confirmed by the experimental results [24]: particle density is reduced when using cw (controlled continuous wave) CO_2 laser processed $YBa_2Cu_3O_7$ target, where the target is being compacted and densified by the irradiation of the laser, and when incorporating certain amount of silver into the targets, where the thermal conductivity of the target is improved. Timm and coworkers [25] have shown that particulate ejection could be sufficiently reduced by advancing the target between laser shots to minimize the morphological changes on the repeatedly irradiated target surface. Similarly, using a molten target could also help to maintain a smooth surface even under the repetitive laser radiation, and therefore eliminate the exfoliation [26,27].

All the solutions mentioned earlier are “active” approach, i.e., to suppress or eliminate the production of particulates in the first place. There are also “passive” approaches proposed, for which, the goal is to remove the particulates from the plume before they reach the

substrate surface. For example, *mechanical particle filtering* is using a velocity selector, which is placed between the target and the substrate and acts as a high-velocity pass filter so that the slow moving particulates could be removed from the plume. *Plume manipulation* includes using two synchronized streams of pulsed laser generated plume or directing the plume onto a hot screen, etc. [3].

2.2.3 Mechanisms of Pulsed Laser Deposition Process

Although PLD is conceptually and experimentally simple, the underlying ablation process is very complicated. When the laser beam hits the target surface, the electromagnetic energy is absorbed and immediately converted to the electron energies, and then into thermal energies by electron-phonon (e-p) coupling to cause evaporation. The e-p coupling could take place down to the light penetration depth L ($L=1/\alpha$, where α is the optical absorption coefficient). If the laser duration time τ is shorter than the time needed for e-p coupling (around 10 picoseconds (ps)), as in the case of picosecond and femtosecond pulsed laser deposition, the conventional heat deposition can no longer play a significant role [28]. If τ has a time scale larger than this, as in the case of nanosecond laser adopted by most of the today's PLD works, then the material ablation occurs exclusively via conventional heat deposition. The thermal diffusion length, according to Fick's law, is given by equation $2(D\tau)^{1/2}$, where D is the thermal diffusion constant. For ceramic material, the light penetration depth L is usually larger than the thermal diffusion length due to its relatively low absorption and low thermal diffusion coefficients. Under this condition, the target will be heated down to the light penetration depth independent of the laser pulse duration. In the case of metallic material, the small light penetration depth and the large thermal diffusion length lead to the opposite

situation: the energy from the laser pulse will be first transferred into the absorption layer, and then thermally transported to a depth of $2(D\tau)^{1/2}$ [29, 30].

However, for most often used nanosecond (ns) pulsed laser deposition, the situation is complicated by a phenomenon called laser-supported absorption (LSA) [6, 10, 25, 29, 30]. With sufficient high laser power density, significant surface evaporation occurs after the first 100 ps of a nanosecond pulse. The localized surface plasma generated would block the energy carried in the remainder of the pulse from being transferred deeper into the bulk target materials. This energy will, instead, go into heating of the plasma. Understandably, when laser-supported absorption dominates, only a small amount of material is ablated since the effective thermal diffusion length is significantly reduced, from $2(D\tau)^{1/2}$ to $2(D\tau_{eff})^{1/2}$ [29, 30]. Singh and Narayan classified the physical process of PLD into three separate stages [6,10]: (i) interaction of the laser beam with the bulk target, (ii) plasma formation and initial three-dimensional isothermal expansion, and (iii) further adiabatic expansion of plasma, which leads to deposition of thin films. The first two stages occur during the time interval of the laser pulse, while the last stage initiates after the laser pulse terminates.

The plasma absorption primarily occurs by an inverse bremsstrahlung process that involves absorption of a photon by a free electron [6, 10, 29]. The absorption coefficient depends on the concentration of the ionized species, plasma temperature, and the frequency of the laser, etc. as expressed in the following equation [31]

$$\alpha_{IB} = 3.7\times10^{8}\frac{Z^{3}n_{i}^{2}}{T^{1/2}\gamma^{3}}(1-e^{-h\gamma/kT}) \tag{2.11}$$

where Z, n_i and T are the average charge, ion density (in cm^{-3}), and the temperature of the plasma (in K), respectively. h, k and ν are Plank constant, Boltzmann constant, and the frequency of laser. It was found that for most materials, after a nanosecond laser pulse, the degree of ionization of the plasma is much higher than that predicted by the Langmuir-Saha equation [6, 10]. Different mechanisms may play an important part in the ionization of the laser–generated species. Processes like impact ionization, photoionization, thermal ionization and electronic excitation, etc., may greatly affect the density of the ionized species [6].

At higher energy density, there exists a self-regulating regime near the target surface: if the absorption of laser by plasma becomes higher, then the evaporation of materials from the target, and therefore the density of ionized species, becomes less, which will reduce the absorption [6, 10]. Since the plasma absorption is proportional to the square of ion density, the strong absorption of plasma only occurs near the target surface, where the density of ionized species is very high. There exists a layer in contact with the target called Knudsen layer, where the collisions between particles tend to equilibrate the plasma and lower the ionization.

Plasma laser supported absorption results in a low ablation yield of highly thermally excited species with kinetic energies ranging from a few eV (neutrals) to more than 100 eV (ions) [32] at temperatures on the order of 2×10^4 K [25]. These energies enhance the mobility of deposition species and result in higher quality thin films, which will be discussed in Section 2.3.2 in details.

Singh and Narayan [6, 10] have developed a theoretical model to simulate the laser-plasma-solid interaction. The plasma is treated as an ideal gas at high pressure and temperature,

which is initially confined in small dimensions, and is suddenly allowed to expand in vacuum. This model successfully predicts most of experimentally observed features on the thin films prepared by pulsed laser deposition, such as the effect of pulsed laser energy density on atomic velocities, the characteristic spatial thickness and compositional variations in multicomponent films as a function of energy density, the dependence of the atomic velocities with atomic weights of various species in multicomponent films, and the thickness and compositional variations as a function of substrate-target distance and irradiated spot size, etc.

References

1. D. Dijkkamp, T. Venkatesan, X. D. Wu, S. A. Shaheen, N. Jisrawi, Y. H. Min-Lee, W. L. McLean, and M. Croft, Appl. Phys. Lett. **51**, 619 (1987).

2. J. Narayan, N. Biunno, R. Singh, O. W. Holland, and O. Auciello, Appl. Phys. Lett. **51**, 1845 (1987)

3. J. T. Cheung, in *Pulsed Laser Deposition of Thin Film,* edited by D. B. Chrisey and G. K. Hubler (Wiley, New York), pp. 1-19 (1994)

4. D. H. Lowndes, D. B. Geohegan, A. A. Puretzky, D. P. Norton, and C. M. Rouleau, Science, **273**, 898 (1996)

5. D. P. Norton; B. C. Chakoumakos; J. D. Budai; D. H. Lowndes; B. C. Sales; J. R. Thompson; D. K. Christen, Science, **265**, 2074 (1994)

6. R. K. Singh and J. Narayan, Phys. Rev. B **41**, 8843 (1990).

7. R. M. Mayo, J. W. Newman, A. Sharma, Y. Yamagata, and J. Narayan, J. Appl. Phys. **86**, 2865 (1999).

8. J. Krishnaswamy, A. Rengan, J. Narayan, K. Vedam, and C. J. McHargue, Appl. Phys. Lett. **54**, 2455 (1989).

9. J. J. Cuomo, D. L. Pappas, J. Bruley, J. P. Doyle, and K. L. Saenger, J. Appl. Phys. **70**, 1706 (1991).

10. R. K. Singh, O. W. Holland, and J. Narayan, J. Appl. Phys. **68**, 233 (1990)

11. S. M. Green, A. Piqué, and K. S. Harshavardhan, in *Pulsed Laser Deposition of Thin Film*, edited by D. B. Chrisey and G. K. Hubler (Wiley, New York), pp. 23-54 (1994)

12. T. Venkatesan, in *Pulsed Laser Deposition of Thin Film,* edited by D. B. Chrisey and G. K. Hubler (Wiley, New York), pp. 313-325 (1994)

13. F. Beech, and I. W. Boyd in *Photochemical Processing of Electronic Materials* (edited by I. W. Boyd), Academic Press, New York, pp. 387-429 (1991)

14. K. L. Saenger, in *Pulsed Laser Deposition of Thin Film,* edited by D. B. Chrisey and G. K. Hubler (Wiley, New York), pp. 581-604 (1994)

15. W. A. Weiner, Appl. Phys. Lett. **52**, 2171 (1988)

16. R. K. Singh, D. Bhattacharya, and J. Narayan, Appl. Phys. Lett. **57**, 2022 (1990)

17. R. K. Singh, D. Bhattacharya, and J. Narayan, MRS 201, 322 (1991)

18. S. Otsubo, T. Minamikawa, Y. Yonezawa, A. Morimoto, and T. Shimuzu, J. Appl. Phys. **29**, L73 (1990)

19. T. Venkatesan, X. D. Wu, A. Inam, and J. B. Watchman, Appl. Phys. Lett. **52**, 1193 (1987)

20. R. A. Neifeld, S. Gunapala, C. Liang, S. A. Shaheen, M. Croft, J. Price, D. Simons, and W. T. Hill III, Appl. Phys. Lett. **53**, 703 (1988)

21. J. A. Greer, and M. D., J. Tabat, Vac. Sci. Technol. A **13** (3), 1157 (1995)

22. J. A. Greer and H. J. Van Hook, MRS Symp. **169**, 463 (1990)

23. G. Koren, A. Gupta, R. J. Baseman, M. I. Lutwyche, and R. B. Laibowitz, Appl. Phys. Lett. **55**, 2450 (1989)

24. R. K. Singh, D. Bhattacharya, and J. Narayan, Appl. Phys. Lett. **61**, 483 (1992)

25. R. Timm, P. R. Willmott, and J. R. Huber, J. Appl. Phys., **80**, 1794 (1996)

26. H. Sankur, W. J. Gunning, J. DeNatale, and J. Flintoff, J. Appl. Phys. **65**, 2475 (1989)

27. T. Szörényi, Z. Kántor, Z. Tóth, and P. Heszleret, Appl. Surf. Sci., **138-139**, 275 (1999)

28. R. P. Pronko, S. K. Dutta, D. Du, and R. K. Si ngh, J. Appl. Phys. **78**, 6233 (1995)

29. P. R. Willmott, and J. R. Huber, Rev. Mod. Phys., **72**, 315 (2000)

30. J. Shen, Zheng Gai, and J. Kirschner, Surf. Sic. Rep. **52**, 163 (2004)

31. T. P. Hughes, *Plasmas and Laser Light* (Wiley, New York) (1975)

32. L. Wiedeman, and H. Helvajian, 1991, J. Appl. Phys. **70**, 4513 (1991)

2.3 NUCLEATION AND GROWTH OF THIN FILMS

2.3.1 Three Basic Growth Modes

Thin film growth goes through two stages: nucleation and growth, which involve series of atomic processes, such as deposition, surface diffusion, and chemical binding, etc. Fig. 2-4 schematically illustrates several major atomic processes: (a) deposition of atoms from the vapor on the surface of both bare substrate or existing clusters; (b) surface diffusion of adatoms; (c) nucleation from mobile adatoms; (d) addition of mobile adatoms to the existing clusters; (e) dissociation of clusters, and finally, (f) depending on the vapor pressure, a certain degree of evaporation of the already absorbed atoms from the surface of both substrate and cluster could also take place.

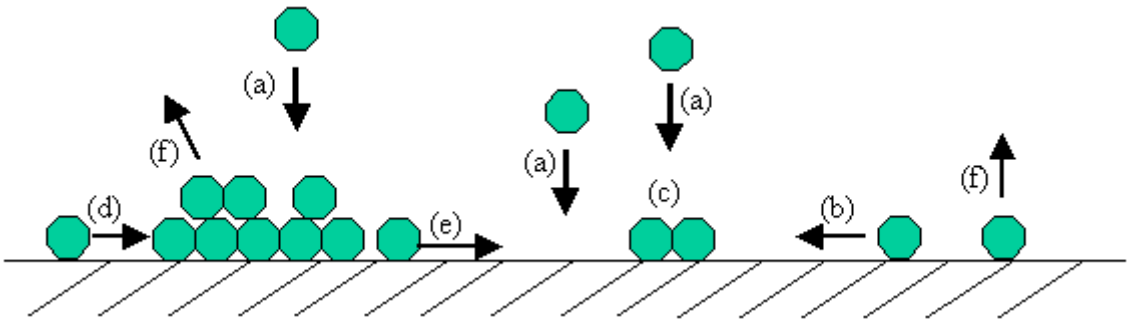

Figure 2-4 Schematic diagram of atomic processes during the thin film growth with (a) deposition, (b) surface diffusion, (c) nucleation, (d) addition to existing clusters, (e) dissociation of clusters, and (f) evaporation.

There are three possible modes of crystal growth on surfaces, which determines the film morphology. These three growth modes are illustrated schematically in Fig.2-5.

(1) Volmer - Weber (island growth, V-W)

In this growth mode, small clusters are nucleated directly on the substrate surface and then grow into three-dimensional islands. With the deposition proceeds, the neighboring islands would coalesce and finally form a continuous film. This mode has been observed in many systems of metals grown on insulators, including many metals on alkali halides, graphite and other layer compounds such as mica [1]

(2) Frank-van der Merwe (layer-by-layer growth, F-M)

At the very beginning, it is similar as that in V-W growth, small clusters are nucleated, but the difference is that those clusters will grow into two-dimensional islands (one monolayer in height). As the deposition proceeds, these two-dimensional islands keep on growing laterally till they coalesce. In other words, the first atoms to condense would form a complete monolayer on the substrate surface before the second layer of film is built up. This growth mode has been observed in many homoepitaxy systems, such as metal on metal, and semiconductor on semiconductor.

(3) Stranski-Krastanov (layer-by-layer followed by island, S-K)

This mode combines the previous two growth modes. After forming the first few monolayers, island growth mode takes over. As a result, islands are formed on the top of a "wetting layer", rather than directly on the bare substrate surface as in the case of V-W

growth. This mode has been observed in many heteroepitaxy semiconductor systems, where a small lattice mismatch exists.

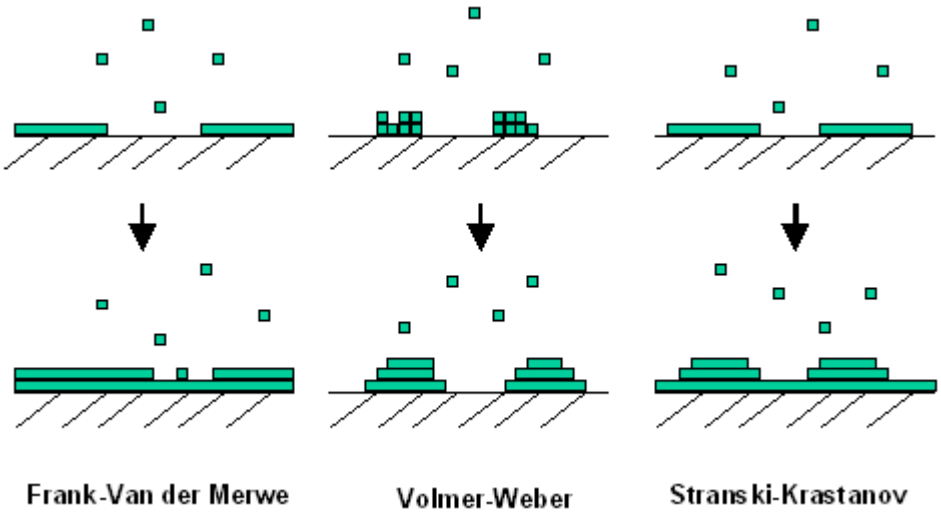

Figure 2-5 Schematic diagram of the three crystal growth modes: Frank-van der Merwe (layer-by-layer growth), Volmer-Weber (island growth), and Stranski-Krastanov (layer-by-layer plus island).

To a large degree, film growth mode is determined by the thermodynamic energy minimization rule. In other words, it is the interplay between the surface free energy of the substrate (σ_s), the surface free energy of the film (σ_f) and the interfacial energy (σ_{int}) that determines which growth mode the system will take. Generally speaking, $\sigma_s = \sigma_f + \sigma_{int}$ favors F-M growth, $\sigma_s < \sigma_f + \sigma_{int}$ favors V-W growth and $\sigma_s > \sigma_f + \sigma_{int}$ favors S-K growth. Equivalently, it could also be explained in the light of atomic bonding. V-W growth takes place if atoms of the deposit (film) material are more strongly bonded to each other than to the substrate atoms, while F-M growth takes place if the atoms of the deposit are more strongly bonded to the substrate than to each other [1]. The reason for the S-K growth to

take place is quite complicated, but it has been commonly accepted that the strain accumulated in the wetting layer makes the system energetically unfavorable to further grow layer by layer, and instead of introducing misfit dislocations, the system takes the island growth mode [2-6].

The above discussion is based on the assumption that the growth proceeds in thermodynamic equilibrium. In practice, however, the film growth is also kinetically controlled in most of the cases, and as a result the growth mode is affected in a certain degree. Kinetic controlling factors includes two aspects: the density of arriving adatoms, which is determined by deposition rate, and the surface mobility of adatoms, which comes from the surface lattice heating, due to (i) a local lattice heating resulted from the combined contributions from the kinetic energy dissipation and the latent heat of condensation [7], and (ii) substrate heating, if any. The adatom surface mobility is strongly affected by the surface defects, which exist in real substrates (e.g., vacancies, steps and kinks), and act as sinks for diffusion atoms, providing them the adsorption sites [8]. The influence of the kinetic parameters on the growth mode will be discussed in the next section in details.

2.3.2 Thin Film Growth by Pulsed Laser Deposition Technique

The deposition characteristics of pulsed laser deposition technique have been found to be significantly different from other vaporization methods. There are two distinguished features: high instantaneous deposition rate and high kinetic energies of the deposited species. These deposition characteristics come from the characteristics of the plasma

generated in PLD process. It was found that the plasma plume density was in the range $1\times10^{13} - 2.0\times10^{14}$ cm^{-3} [9, 10], and the kinetic energies of the ejected species are in the range of several eV up to hundreds of eV.

In film growth, supersaturation is defined as the ratio of the pressure of arriving atoms to the equilibrium vapor pressure, or equivalently, the actual deposition rate to the equilibrium deposition rate at given substrate temperature. Supersaturation is an important thermodynamic parameter that determines, to a great extent, the growth mechanism since it is directly related to the volume free energy per unity volume of clusters formed on the substrate, ΔG_V, by the following equation [11]:

$$\Delta G_V = -\frac{kT}{\Omega}\ln(\frac{P}{P_e}) = -\frac{kT}{\Omega}\ln(\zeta) \tag{2.12}$$

where P, P_e and ξ are the pressure of arriving atoms, the equilibrium vapor pressure (at substrate temperature T) and the supersaturation, respectively. Ω is the atomic volume of the film atoms. Obviously, an increase in the supersaturation leads to an increase in the magnitude of volume free energy ΔG_V. Taking into the considerations of the surface (interfacial) energy increase due to the cluster formation, the critical cluster (nuclei) radius, r^*, and the free-energy barrier for nucleation, ΔG^*, are given by [12]:

$$r^* = \frac{-2(a_1\Gamma_{c-v} + a_2\Gamma_{s-c} - a_2\Gamma_{s-v})}{3a_3\Delta G_V} \tag{2.13}$$

$$\Delta G^* = \frac{4(a_1\Gamma_{c-v} + a_2\Gamma_{s-c} - a_2\Gamma_{s-v})^3}{27(a_3\Delta G_V)^2} \tag{2.14}$$

where Γ represents the interfacial energy with *c*, *s*, and *v* referring to the cluster, the substrate, and the vapor, respectively. For a given substrate-film system (Γ_s are set), an increase in the magnitude of volume free energy ΔG_V, in turn, leads to a decrease in the size of critical nuclei and the nucleation barrier, and therefore, an increase in the nucleation rate.

The preceding discussion shows that the high instantaneous deposition rate resulting from the highly saturated plume in PLD leads to a smaller critical nucleus size, a higher nucleation rate and a higher nuclei density.

Another important feature of pulsed laser deposition is the high kinetic energies of the depositing species. Studies showed that the ions can have kinetic energies up to 1000 eV (with an average 350 eV) while neutrals are much slower than the ions with kinetic energies of 5-10 eV. In comparison, the kinetic energies of impinging atoms in MBE are only 0.1 eV [7, 13]. One direct result of the kinetic energies of impinging atoms, which is desired by the growth of high quality film, is the enhanced adatom mobility [14]. The adatom mobility comes from the local surface lattice heating due to the combined contributions from the kinetic energy dissipation and the latent heat of condensation. While it is negligibly small in MBE, the kinetic energy dissipation in PLD is comparable to the latent heat of condensation [7]. One of the advantages of PLD due to the enhanced adatom mobility is the lowering of epitaxial growth temperature. In epitaxial growth, the diffusivity of adatoms must be high enough so that the adatoms could migrate to the thermodynamically stable sites to minimize

the total energy. For other deposition techniques, in which the kinetic energy is low, such as MBE, increasing the substrate temperature is the only way to enhance the adatom mobility. Sankur and coworkers [15] showed that the heteroepitaxial growth of germanium was possible at 300 ˚C using PLD, while for MBE growth, temperatures above 700˚C are required. In addition, the successful growth of diamond-like carbon (DLC) with high sp^3*:* sp^2 ratios by PLD is also attributed to the deposition of energetic ablated species [9, 10,16].

The impinging of atoms with high kinetic energies also could lead to local defect formation. The molecular dynamic simulations by Krebs, *et al*. [13] showed that the impingement of particles with kinetic energies less than about 10 eV (as the case of the atoms during pulsed laser deposition) only enhances the adatom mobility without causing any defect formation. When the kinetic energy reaches 15 eV, the surface defect would form in the as-deposited layer, and with the kinetic energy further being increased, the bulk displacements, and even the implantation of particles would take place.

For a given PLD system, the laser power density, repetition rate, and the spot size are the main parameters that affect the film growth quality. While the instantaneous deposition rate could be controlled by adjusting the laser fluence and spot size, the average deposition rate is mainly determined by the laser repetition rate. In order to avoid the formation of the surface defects and the incorporation of particulates to the deposited film, the laser fluence should be kept slightly above the ablation threshold.

References

1. J. A. Venables, G. D. T. Spiller, and M. Hanbucken, Rep. Prog. Phys. **47**, 399 (1984)
2. Serge Luryi, and Ephraim Suhir, Appl. Letts., **49**, 140 (1986)
3. D. J. Eaglesham, and M. Cerullo, Phys. Rev. Letts., **64**, 1943 (1990)
4. J. Tersoff, and F. K. LeGoues, Phys. Rev. Letts., **72**, 3570 (1994)
5. S. Christiansen, M. Albrecht, H. P. Strunk, P. O. Hansson, and E. Bauser, Appl. Phys. Letts., **66**, 574 (1995)
6. L. J. Gray, M. F. Chrisholm, and Theodore Kaplan, Appl. Letts., **66**, 1924 (1995)
7. J. Shen, Zheng Gai, and J. Kirschner, Surf. Sic. Rep. **52**, 163 (2004)
8. R. Koch, J. Phys.: Condens. Matter, **6**, 9519 (1994)
9. R. M. Mayo, J. W. Newman, A. Sharma, Y. Yamagata, and J. Narayan, J. Appl. Phys. **86**, 2865 (1999)
10. R. M. Mayo, J. W. Newman, Y. Yamagata, A. Sharma, and J. Narayan, J. Appl. Phys. **88**, 6868 (2000)
11. J. S. Horwitz, and J. A. Sprague, in *Pulsed Laser Deposition of Thin Film*, edited by D. B. Chrisey and G. K. Hubler (Wiley, New York), pp. 229-254 (1994)
12. J. E. Greene, in *Multicomponent and Multilayered Thin Films for Advanced Microtechnologies* (edited by O. Auciello and J. Engemann), NATO/ASI Series E, Kluwer Academic Publishers, The Netherlands, **234**, 39 (1993)
13. H. U. Krebs, M. Störmer, S. Fähler, O. Bremert, M. Hamp, A. Pundt, H. Teichler, W. Blum and T. H. Metzger, Appl Surf. Sci. **109/110**, 563 (1997)
14. J. P. Zheng, Z. Q. Huang, D. T. Shaw, and H. S. Kwok, Appl. Phys. Lett., **54**, 280 (1989)
15. H. Sankur, W. J. Gunning, J. DeNatale, and J. Flintoff, J. Appl. Phys. **65**, 2475 (1989)
16. Douglas H. Lowndes, D. B. Geohegan, A. A> Puretzky, D. P. Norton, C. M. Rouleau, Science, **273**, 898 (1996)

3 EXPERIMENTS

3.1 GROWTH

Growth was conducted in a pulsed laser deposition system with KrF laser (248 nm, 25 ns). The top view of the experimental set-up is schematically illustrated in Fig. 3-1. The laser beam is directed into the vacuum chamber and focused on the target surface at an incident angle of 45° by a set of optical components (mirror, lens, etc.), resulting in a plume ejected from the target surface at a high speed. The species carried in the plume is directly deposited on the substrate surface, which is positioned parallel to the target surface at distance of 4 cm. The substrate could be heated and the temperature is monitored by a thermal couple. The target holder can hold up to four targets, and therefore, it is quite straightforward to make multilayered structures in this system. A small driving motor is connected to the target holder to rotate the target during the deposition, as a result, the surface where the laser beam hits continuously changes, which is believed to be an effective way to reduce the exfoliation [1].

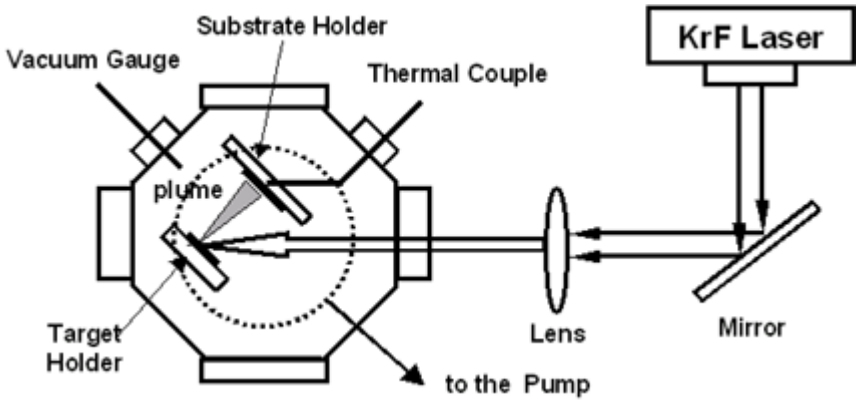

Figure 3-1 Schematic diagram of the set-up of pulsed laser deposition system (top view)

The energy density deposited on the target surface could be adjusted by the output laser power as well as the spot size (through adjusting the lens position). When the laser fluence is fixed, the film thickness profile becomes more forward peaked as the spot size increases [2]. Therefore in this work, the spot size was kept as the smallest so that the film uniformity is optimized, which is crucial to the nanostructure growth since their size is directly determined by the nominal thickness of the deposited material.

Before deposition, the silicon substrates were ultrasonically degreased and cleaned in acetone and methanol for 5 ~ 10 minutes, which was followed by a short time etching in a hydrofluoric acid solution (49 % HF) to remove the surface silicon dioxide layer, forming hydrogen-terminated surface.

The template layer TiN/Al_2O_3 and Ni were deposited successively on the hydrogen-terminated silicon (001) substrate by ablating a hot pressed TiN/Al_2O_3 target and a pure nickel target, respectively. The base pressure for all the depositions was lower than $1x10^{-6}$ Torr, and after substrate heating, the pressure increases to 10^{-6} Torr range. The main deposition parameters are listed in Table 3-1

Table 3-1 Pulsed laser deposition parameters

	Laser Energy Density	Repetition Frequency	Temperature (°C)	Deposition Time
Ni	4 J/cm^2	10 Hz	400 ~ 700	20 sec ~ 3 min
TiN	4 J/cm^2	10 Hz	600	~ 2 min
Al_2O_3	4 J/cm^2	5 Hz	300	20 sec[a]/ 1 min[b]

a: for capping

b: for multilayer structures

The energy density for nickel deposition was set to be around 4 J/cm^2 since it is a transition metal and the deposition requires relatively higher ablation threshold [3]. For studying the effect of deposition temperature on the nickel crystal growth, the deposition temperature for nickel was varied in the range of 400 °C to 700 °C. The size of Ni particles was expected to vary with the nominal thickness of nickel layer (the amount of material being deposited), which was adjusted by varying the deposition time ranging from 20 seconds to 3 minutes.

In order to minimize the effects of the template crystalline quality on the nickel crystal growth, the deposition temperature for titanium nitride was fixed between 600 °C to 650 °C, an optimized deposition temperature range for titanium nitride epitaxial growth on Si (001) substrate [4-5].

Aluminum oxide serves two roles here, one is as the template to grow crystallographically randomly oriented nickel islands, and the other is as capping material for covering the nickel islands so that the as-deposited island morphology could be preserved.

Multi-layered structures, where layers of nickel islands are separated by TiN or Al_2O_3 layer, were also deposited for the magnetic measurements so that sufficient signal could be obtained.

3.2 STRUCTURAL CHARACTERIZATION

The characterization of the material is a critical step in this study. We employed TEM studies complemented with X-ray diffraction. The principles and advantages are discussed in the following sections.

3.2.1 X-ray Diffraction

X-ray diffraction (XRD) θ-2θ scan was employed to roughly examine the crystalline quality of the samples (both the template and the nanostructures). This measurement provides the crystalline information from a larger area of the sample, which no doubt is strength if compared with TEM study where only a very tiny area is examined. However, since it only gives the texturing information along the growth direction, the determination of an exact orientation relationship is impossible. In addition, the expected height of nanostructures is only around 10 nm, far less than the measurement penetration depth, which leads to a very weak signal. Therefore, XRD θ-2θ scan only serves as a complementary technique for studying the crystallographic orientation in this work.

The crystallographic orientation, shape, as well as the size and lateral spatial distribution of nickel nanostructures, were studied in detail by transmission electron microscopy study (JEOL 2010F and TOPCON 002B). Both cross-sectional and plan-view samples were prepared by mechanical polishing, followed by Ar-ion milling to electron transparency.

3.2.2 Cross-sectional TEM study – Orientation, Shape, and Faceting

The crystallographic orientation was studied in detail by selected area diffraction (SAD), bright-field and central dark-field imaging (BF and CDF), and high-resolution transmission electron microscopy (HRTEM). A cross-sectional SAD pattern taken from area containing both the film and substrate provides relative position of the corresponding lattice planes, and hence makes it possible to determine the exact orientation relationship. HRTEM, on the other hand, gives a lattice image of the epitaxial interface from a specific island/area.

Compared with atomic force microscopy (AFM), which tends to overestimate the lateral dimension and modify the shape of nanostructures due to the tip effect, cross-sectional TEM and HRTEM imaging give more reliable information on island shape and faceting. However, since cross-sectional TEM and HRTEM imaging gives only a projected shape of the islands along the zone axis direction, plan-view study, which provides information on the island base (e.g., shape, edge direction), was necessary.

3.2.3 Plan-view TEM Study – Size and Lateral Spatial Distribution

Although the lateral size and height of nanostructures could be precisely determined in cross-sectional CTEM and HRTEM images, a plan-view study, which could image hundreds of nanostructures at one time, is needed to get a statistical size distribution. In addition, a plan-view image also gives information on the nanostructure lateral distribution. In a conventional plan-view TEM study of epitaxially grown islands, the real shape and size of the islands are often obscured by strain contrast. In this work, scanning transmission electron

microscopy (STEM) Z-contrast imaging technique (Section 3.2.4) was employed to study the plan-view samples.

3.2.4 STEM Z-Contrast Imaging

In STEM, a fine probe is scanned over the sample, which is so thin that electrons transmit through the sample. The transmitted electrons are then detected and displayed on a raster, synchronized with the probe scan. STEM combines the strengths of TEM and SEM (scanning electron microscopy): high resolution and point analysis.

There are three main imaging modes in STEM: (1) bright-field, in which the image is formed with the electrons detected in a small axial detector, (2) dark-field, in which the image is formed with the elastically scattered electrons (e.g., Bragg) collected on an annular detector with a small inner cutoff (usually matched to the illumination aperture), (3) high-angle annular dark-filed (HAADF) Z-contrast image, in which the image is formed with electrons detected by a high-angle annular detector (with larger inner and outer detector cutoff). In HAADF mode, the contribution of elastic Bragg scattering (and hence 'diffraction contrast' artifacts) is reduced, and the contribution of localized thermal diffuse scattering (TDS), sometimes called 'quasi-elastic scattering', is increased. The minimization of Bragg scattering by using sufficiently high-angle detector gives the image with strong mass thickness contrast. The cross-section of the scattering is proportional to the square of the atomic number (Z) according to the Rutherford formula for scattering from an unscreened nucleus, and therefore, the image was also called "Z-contrast" [6]. JEOL 2010 F has both TEM and STEM mode.

The high sensitivity of this imaging method to the atomic number Z makes it a suitable candidate for investigating plan-view samples with the nanostructures (islands) grown on the substrate under Volmer-Weber mode. It is expected to reveal the real size and shape of the island base as well as the island spacing (if the sample is not over thinned), provided that the growth is three-dimensional and there is a significant difference in the average atomic number of the deposited material and the substrate.

3.3 MAGNETIC CHARACTERIZATION

Magnetic properties of the samples were measured using superconducting quantum interference device (SQUID) magnetometer. SQUID is a mechanism used to measure extremely weak signals. A SQUID device consists of a Josephson junction, also called "weak link", which is a superconducting ring with a small portion replaced by a thin insulating layer (the layer is so thin that electrons can tunnel through), as shown in Fig. 3.2 [7]. The resolution of these devices is down to 10^{-14} Tesla (10^{-10} gauss) [8]. Due to its high sensitivity, SQUID is one of the most commonly used characterization techniques for nanostructured magnetic materials.

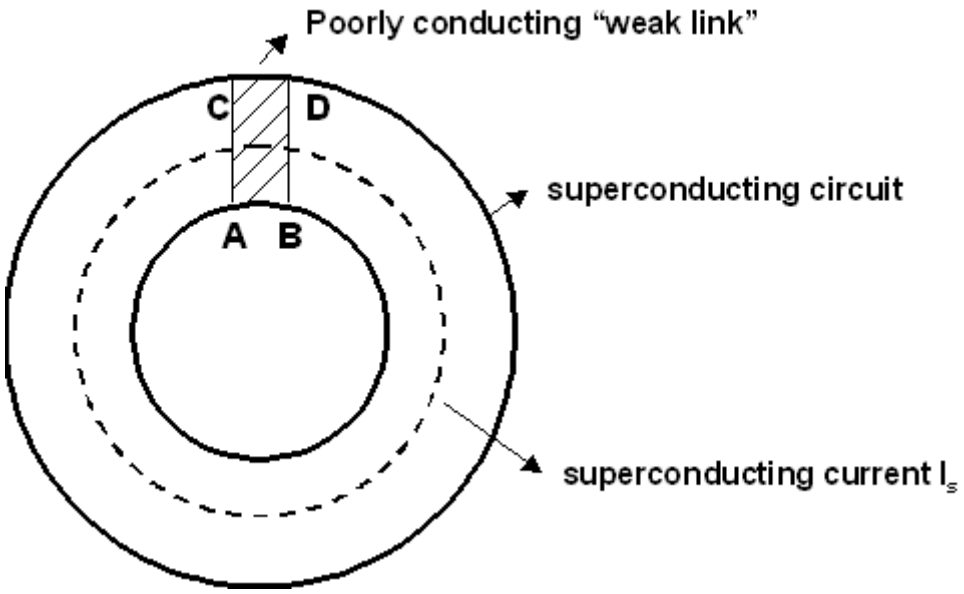

Figure 3-2 A Josephson Junction device, which consists of a superconductor with a poorly conducting "weak link" , A B C D (Ref. [7]).

Two kinds of measurements were conducted, the typical magnetization curves (hysteresis loops) at varied temperatures, and the so-called zero-field-cooling (ZFC), field-cooling (FC) magnetization curves, which are unique for magnetic nanoparticle characterization.

The ZFC and FC magnetization curves are obtained in the following way. First, cool the sample in zero magnetic field from room temperature, where all particles show superparamagnetic behavior, to 10 K. ZFC curve is then obtained by applying a small magnetic field of 50 Oe to the sample and measuring the magnetization when the temperature is increased step by step back to room temperature. After that, at the same small field (50 Oe), cool the sample back to 10 K while measuring the magnetization as a function of temperature, the resulted curve is FC. A distinct feature of ZFC/FC measurements is a peak in ZFC curve, from which, one can extract information about the average blocking temperature, and therefore the anisotropy constant if the mean particle size (volume) is known (refer to section 2.1.2). The difference between the maximum in the ZFC curve and the bifurcation between the ZFC and FC curves give the information on the particle size dispersion.

REFERENCES

1. R Timm, P. R. Willmott, and J. R., J. Huber, Appl. Phys. **80**, 1794(1996)
2. K. Saenger, in *Pulsed Laser Deposition of Thin Film*, edited by D. B. Chrisey and G. K. Hubler (Wiley, New York), pp. 199-228 (1994)
3. J. C. S. Kools, in *Pulsed Laser Deposition of Thin Film*, edited by D. B. Chrisey and G. K. Hubler (Wiley, New York), pp. 455-471 (1994)
4. J. Narayan, P. Tiwari, X. Chen, R. Chowdhury, and T. Zheleva, Appl. Phys. Lett., **61**, 1290 (1992)
5. J. Narayan, U.S. Patent No. 5,406, 123 (1995)
6. John C. H. Spence, in *High-resolution Electron Microscopy*, 3rd edition, Oxford Science Publications, Oxford (2003), Chapter 8, and references therein.
7. David Jiles, in *Introduction to Magnetism and Magnetic Materials*, Chapman and Hall, New York (1991)
8. W. Webb, IEEE Trans. Mag., **8**, 51(1972)

4 NICKEL SELF-ASSEMBLED GROWTH

4.1 GROWTH MODE

Shown in Fig. 4.1 are the representative cross-sectional <011> zone axis low magnification images of the samples where nickel was deposited at varied temperatures. It is seen that whereas titanium nitride formed a continuous layer on the silicon substrate, nickel exhibited an obvious island growth mode in the whole temperature range under investigation (400 °C to 650 °C). Hereafter, the term "island" will be used to denote these nickel nanostructures. Z-contrast imaging is highly sensitive to the atomic number (the intensity is proportional to the square of the atomic number if the thickness is constant). Therefore, the fact that there is no wetting layer observed in Z-contrast images, as shown in Fig. 4.1(c), indicates that the growth of nickel on epitaxially grown titanium nitride is three-dimensional in accordance with V-W mode.

Images as shown in figure 4.1 were also used to determine the island shape. It is clearly seen that all the nickel islands are faceted with well-defined shapes. A truncated pyramidal shape is the most commonly observed one (Fig. 4.1 (a) and (c)). Whereas non-truncated pyramidal (triangular shaped) islands were also observed in some samples (Fig. 4.1 (b)). The appearance of these different morphologies is found to be related to the template crystalline quality and the deposition conditions, which will be discussed later in Section 4.3.

The lateral size of islands varies from a few nanometers to tens of nanometers, depending on the deposition time chosen. Some large-sized islands observed in samples apparently result

from the coalescence between neighboring islands. The height distribution of islands is much narrower than that of lateral size. The height/lateral size aspect ratio did not show strong temperature dependence in the temperature range of the investigation. The separation between islands is expected to be larger than it appears in the cross-sectional TEM image due to the projection overlapping.

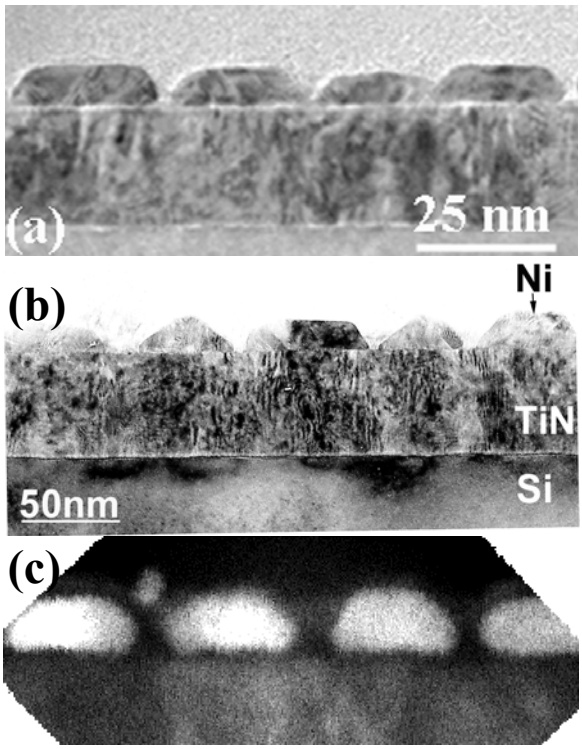

Figure 4-1 Images of nickel islands grown on titanium nitride template layer: (a) and (b) low-magnification CTEM images with (a) grown at 400 ˚C for 30 seconds and (b) grown at 600 ˚C for 45 seconds; (c) STEM Z-contrast image (30 seconds at 400 ˚C). All the images were taken in Si <110> zone axis.

During epitaxial growth, which growth mode the deposited material adopts is determined by the surface free energy of both substrate and film material, and the interfacial energy as well. For a heteroepitaxial system, the interfacial energy has two contributions: (1) interfacial atomic bonding strength, i.e., chemical bonding strength between the two materials, which is closely related to the electronic structure of the interface atoms and the atomic configuration of the interface, and (2) the lattice strain due to the lattice misfit. The crystal structure and the lattice constant of silicon, titanium nitride, and nickel are listed in Table 4-1. If assuming both titanium nitride and nickel are all epitaxially grown by "cube-on-cube" orientation, which will be discussed and confirmed in the next section, then the misfit of TiN/Si and Ni/TiN is 22% and 17%, respectively. The fact that TiN/Si took F-M growth mode while has greater lattice misfit than Ni/TiN, which took V-W growth mode, suggests that the misfit here did not play a critical role in the energetics. This might not be surprising if considering that both TiN and Ni were grown by domain matching epitaxy, where arrays of dislocations were introduced to the interface in the very beginning of the growth. The nucleation barrier for misfit dislocations decreases strongly with increase in magnitude of the misfit [1]. Therefore, very likely, as long as the misfit exceeds such a value that the misfit dislocations nucleated right in the interface, then the dependence of the interfacial energy on the lattice misfit becomes much less significant. In other words, the interfacial energy is not necessarily proportional to the interfacial dislocation density. Certainly, the above discussion is only valid to the systems with large lattice misfit, for those systems with small misfit, e.g., $< 7 \sim 8$ %, the lattice misfit still plays a critical role in interfacial energetics.

Table 4-1 The crystal structure and the lattice constant of silicon, titanium nitride and nickel

Materials	Silicon	Titanium Nitride	Nickel
Crystal Structure	Diamond fcc at (0,0,0; ¼, ¼, ¼)	Sodium Chloride fcc at (0,0,0; 1/2, 1/2, 0)	fcc at (0,0,0)
Lattice constant (Å)	5.43	4.24	3.52

There are very few data of the interfacial energy reported in literature. This is partially because the experimental techniques available are limited and theoretical calculations need the exact information about the atomic configuration and the strain states, which vary for each individual system.

Here the growth condition will be examined only in light of the surface energy of both the substrate and the film, assuming that interfacial energy is fixed. The data on the surface free energy as a function of orientation in the literature were mostly theoretically calculated, and thus values depend strongly on which theory, model and assumptions they were based on. Therefore, one cannot compare the absolute values from different sources where different calculation techniques were used. However, it should give the right estimates if the comparison is done for the data from the same source. Table 4-2 lists the surface free energies for some low index facets of silicon, titanium nitride and nickel obtained from the literature [2-4]. There is a significant difference in the surface energy between the different facets of TiN, a phenomenon not found in silicon and nickel. Even unrelaxed TiN (100)

surface has a relatively low surface free energy, around 1.53 to 1.76 Jm^{-2}, while that of TiN (110) and TiN (111) are several times higher (2.87 to 3.14 Jm^{-2} for (110) and 5.08 to 5.45 Jm^{-2} for (111)) [3]. This could partially explain our result that TiN has a very strong tendency to epitaxially grow on Si (100) by Frank-van der Merwe mode (two-dimensional), while on the top of TiN (100), Ni tends not to wet the low energy stable surface by growing in Volmer-Weber mode (three-dimensional). The fact that deposited nickel takes an island growth mode could also be explained by the surface energy data of nickel itself [4]: among the different facets of nickel crystal, it is the (111) facet, rather than the (100) facet, which has the lowest surface energy. The surface energy anisotropy of nickel is also the determining factor for the island faceting, which will be discussed later in detail.

Table 4-2 Surface energy values obtained from the references [2-4]

Materials	Surface Energies (Jm^{-2})			Method	Reference No.
	100	110	111		
Si	1.36	1.43	1.23	Experiments	
	1.34	1.573	1.41	Calculations	2
	1.488	1.721	1.405	Calculations	
TiN	1.06 [a], 1.53 [b]	2.59 [a], 2.87 [b]	4.59 [a], 5.08 [b]	GGA[c], RPBE [d]	3
	1.28 [a], 1.75 [b]	2.85 [a], 3.13 [b]	4.92 [a], 5.42 [b]	GGA[c], PBE[d]	
	1.30 [a], 1.76 [b]	2.86 [a], 3.14 [b]	4.95 [a], 5.45 [b]	GGA[c], PW91[d]	
Ni	2.426	2.368	2.011	GGA[c], FCD [e]	4

"a" — for relaxed geometries

"b" — for unrelaxed geometries

"c" — generalized gradient approximation

"d" — refer to different functional forms used for GGA, check the corresponding reference for details

"e" — full charge density

4.2 EPITAXIAL ORIENTATION

A typical X-ray diffraction (XRD) pattern of a deposited sample is shown in Fig. 4.2. Since there is no other diffraction peak observed except TiN (200), TiN (400) and Ni (200), it is reasonable to conclude that both TiN and Ni are highly textured along the growth direction, which is Si <001> direction. It should be noticed that θ -2θ scan provides information on alignment only in the direction normal to the surface.

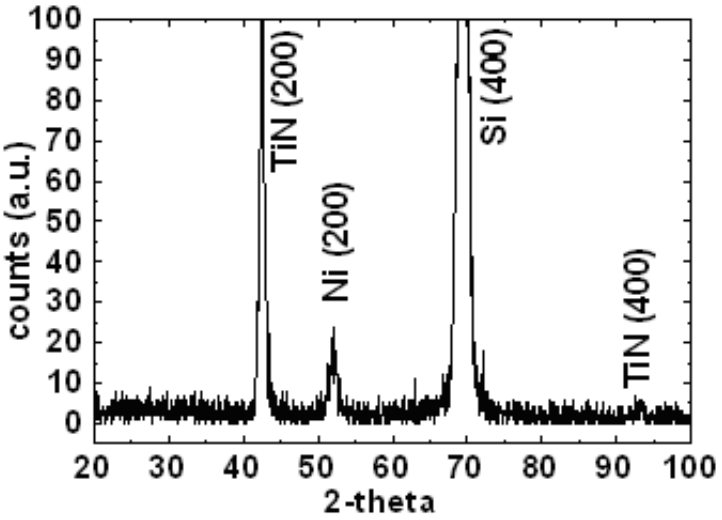

Figure 4-2 X-ray diffraction pattern from a sample with a layer of nickel islands grown on silicon (001) substrate using epitaxial titanium nitride as the template. No other diffraction peak is observed except TiN (200), TiN (400) and Ni (200), indicating that TiN and Ni are highly textured along the growth direction.

Results obtained from TEM SAD studies, which can provide the alignment information in all three directions, are shown in Fig 4.3 (<011> cross-sectional) and Fig. 4.4 (<001> plan-view). The area examined contains silicon, titanium nitride and nickel. The alignment of

diffraction spots of Si, TiN and Ni in Fig. 4-3 indicates that the predominant epitaxial orientation for both TiN and Ni is "cube-on-cube", i.e., all three <100> axes of films are parallel to those of silicon substrate. In Fig. 4-4, due to the selection rules in diamond structure, Si (200) did not appear, but Si (400) and Si (220) spots do align with that of TiN. Nickel diffractions did not show up, probably because its volume is too small, which leads to very weak signals. The "arced-shape" of TiN diffraction spots indicates the in-plane misorientation of TiN, which is about a few degrees. In addition, sets of the spots due to double diffractions between silicon and titanium nitride also appeared, which further confirms the epitaxial orientation relationship.

This "cube-on-cube" orientation relation can be also clearly seen from the interface high-resolution image (Fig. 4-5 (a)) and its corresponding Fast Fourie Transform (FFT) pattern (Fig.4-5 (b)).

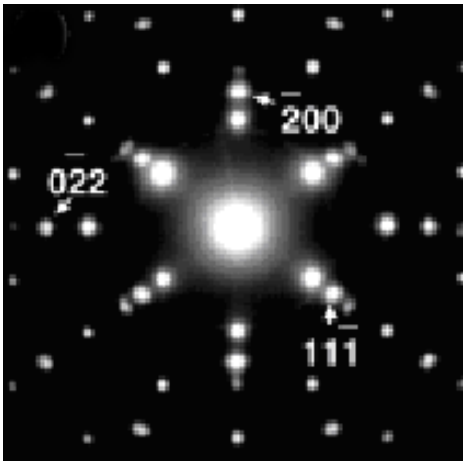

Figure 4-3 Cross-sectional <011> zone axis SAD pattern taken from an area containing silicon substrate, titanium nitride template and nickel islands.

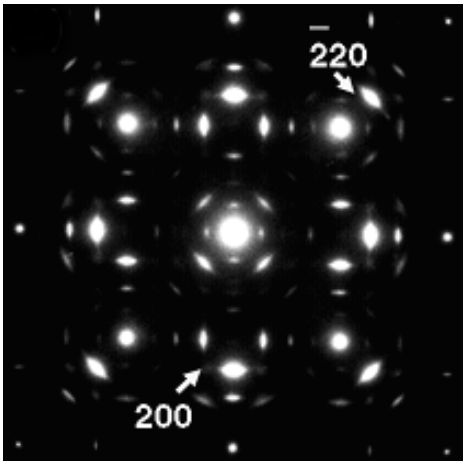

Figure 4-4 Plan-view <001> zone axis SAD pattern taken from an area containing silicon substrate, titanium nitride template and nickel islands.

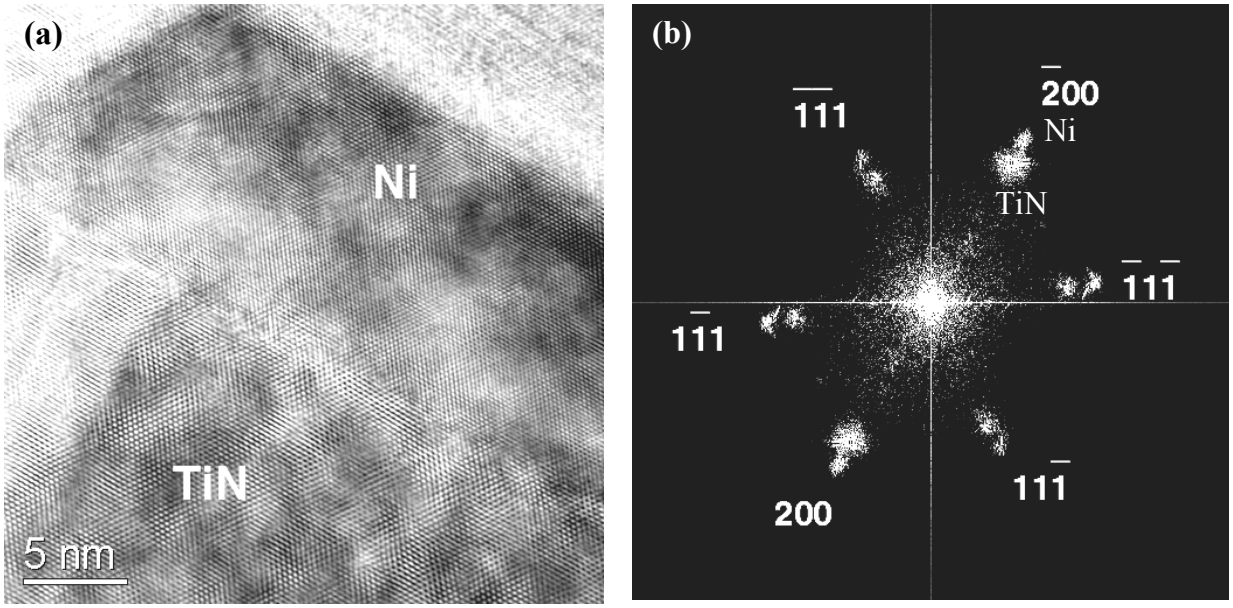

Figure 4-5 (a) High-resolution TEM image of a truncated pyramid shaped nickel island taken from Si <011> zone axis; (b) The corresponding FFT pattern indicates the cube-on-cube epitaxial growth.

As listed in Table 4-1, silicon has a diamond structure with a lattice constant 0.543 nm and titanium nitride has a sodium chloride structure with a lattice constant 0.424 nm. Their lattice mismatch is as large as 22%. The epitaxial growth of titanium nitride on Si (100) is achieved by domain matching epitaxy (DME) mechanism, where integral multiples of major lattice planes match across the interface [5-6]. The misfit between nickel, which has a simple face-centered cubic (fcc) structure with a lattice constant of 0.352 nm, and titanium nitride is 17%, far beyond the critical strain (7%-8%) of conventional one-to-one lattice mismatching. Therefore, domain-matching epitaxy should also be expected for nickel island growth, which was indeed observed. An amplified <011> zone axis HRTEM image of Ni/TiN interface shown in Fig. 4-6 clearly shows the misfit dislocations distributed along the interface. The small black arrows indicate the extra (111) lattice planes.

The domain size varies a lot, from 4TiN/5Ni, 5TiN/6Ni to 6TiN/7Ni and even 7TiN/8Ni. The variation is possibly due to two reasons: local topographical features in the TiN surface, such as steps, and the special nature of 3D island growth, in which the dislocations may be generated at the edge of islands [7-10]. The first reason is more likely true since in HRTEM images of the interface, steps are indeed seen accompanied by a significant change of domain size. The Burgers vector of those dislocations is $\frac{a}{2}\langle 110\rangle$ lying in (111) planes (60° dislocation). The dislocations usually appear in pairs (in two sets of (111) plane) and combine at the interface to form a 90° dislocation with Burgers vector $\frac{a}{2}\langle 110\rangle$ lying in (100) plane.

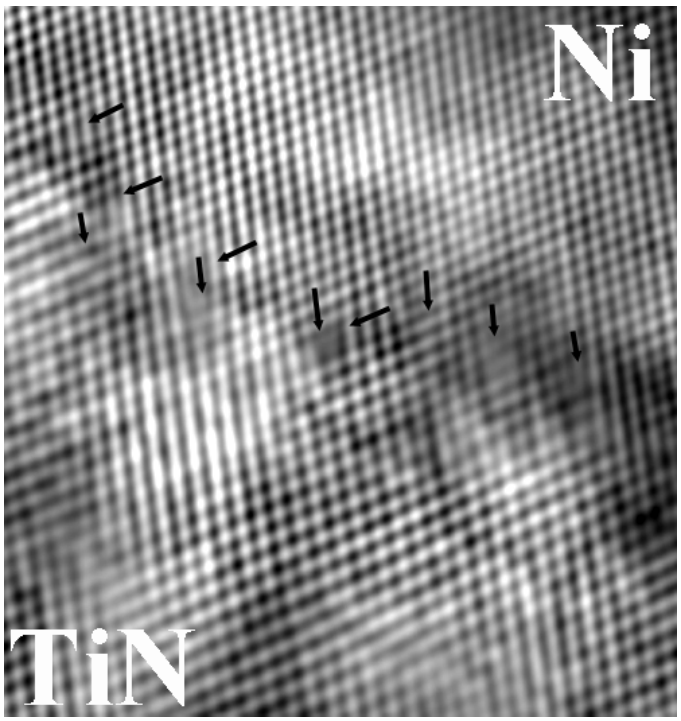

Figure 4-6 Amplified <011> zone axis HRTEM image of the interface between a cube-on-cube oriented nickel island and the titanium nitride template. Small black arrows indicate extra (111) lattice planes. It is clearly seen that these are 60° dislocations with a Burgers vector $\frac{a}{2}\langle 110\rangle$ *lying in (111) planes. Some of dislocations appear in pairs combining at the interface to form a 90° dislocation with Burgers vector* $\frac{a}{2}\langle 110\rangle$ *lying in (100) plane.*

Other orientations for nickel island growth have been also observed. In most cases, the (111) planes of nickel crystallites tilted themselves about a certain angle toward the TiN/Ni interface. From the crystallographic point of view, this orientation is the result of a rotation of nickel crystallites (typically by 83° or 90°) on one of TiN <011> directions parallel to the interface (zone axis of cross-sectional TEM study). This kind of orientation will be called "rotational orientation" hereafter. Fig. 4-7 and Fig. 4-8 show HRTEM images of islands

grown via rotational orientation relationship, whereas Fig. 4-9 is a schematic illustration of the rotation relationship.

In the case of heteroepitaxial thin film growth, there are several factors that will affect the epitaxial orientation, such as lattice misfit, interfacial atomic bonding, and even the adatom mobility, which is determined by both the thermal energy of the adatoms and the substrate surface local roughness (topographical features of the substrate, e.g., steps). In all cases where nickel grows via rotational orientation, two sets of (111) planes have tilted themselves to form a different inclination angle θ with respect to the template surface compared to that of the cube-on-cube case. Therefore, it is very straightforward to estimate the lattice misfit by considering {111} plane matching at the interface, as schematically shown in Fig. 4-10.

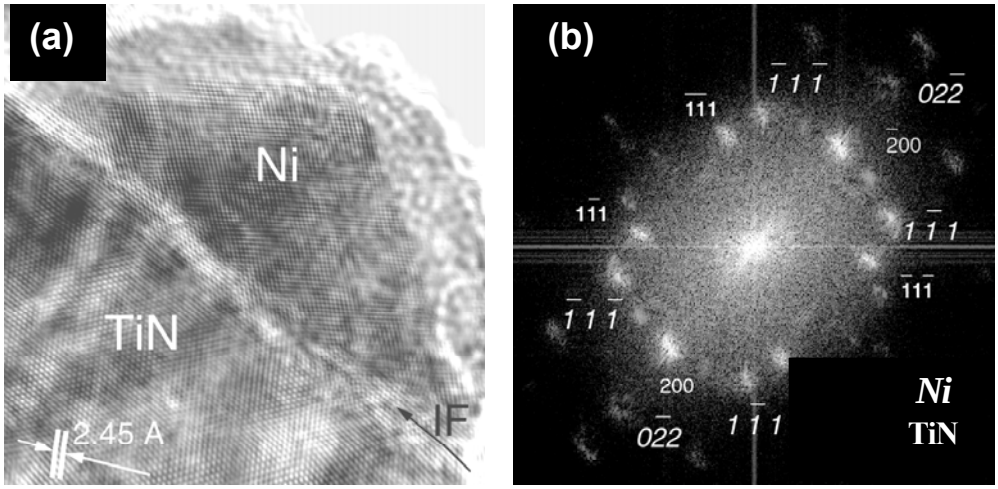

Figure 4-7 (a) HRTEM image of a nickel island taken from Si <011> zone axis; (b) the corresponding FFT pattern indicates the 90º rotation epitaxial growth. Indexes in smaller regular numbers and bigger oblique numbers are referring to TiN and Ni, respectively.

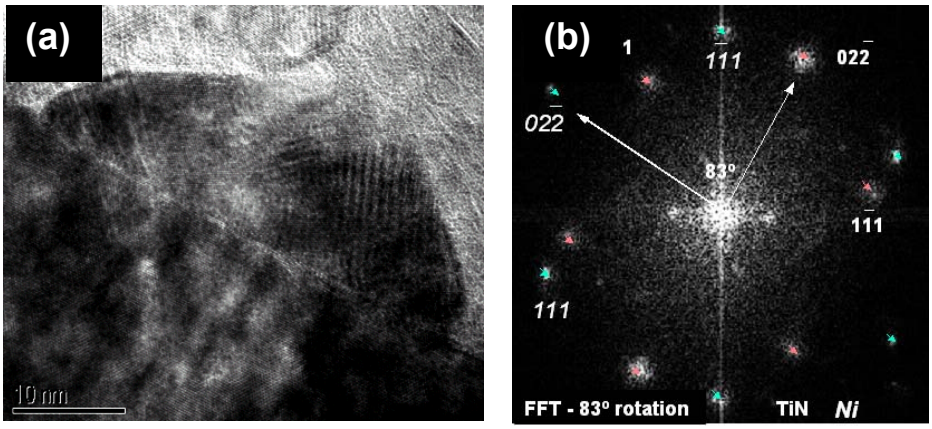

Figure 4-8 (a) HRTEM image of a nickel island taken from Si <011> zone axis; (b) the corresponding FFT pattern indicates the 83º rotation epitaxial growth. Indexes in smaller regular numbers and bigger oblique numbers are referring to TiN and Ni, respectively.

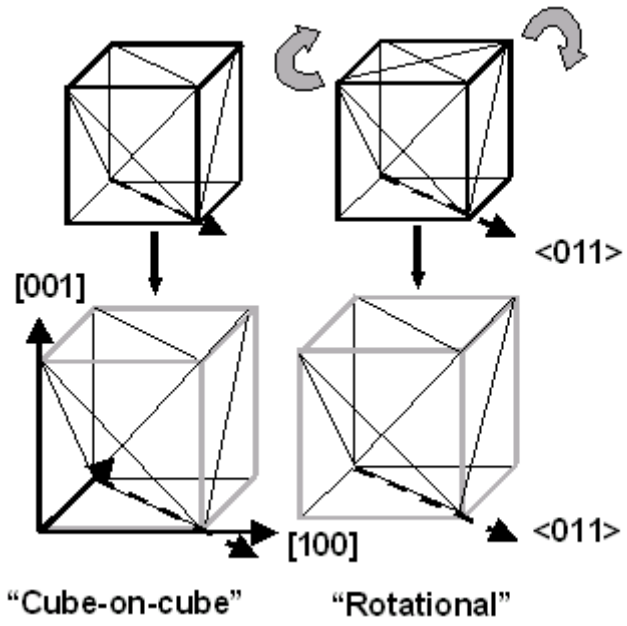

Figure 4-9 Schematics of "cube-on-cube" and "rotational"orientation relationships

Table 4-3 lists the inclination angle θ and the resulting misfit in these three orientations: "cube-on-cube", "90˚ rotation", and "83˚ rotation". Obviously, in both rotation modes, the inclination angle θ is decreased, which however, according to the calculation, did not lead to the reduction of the misfit as expected. In fact, the misfit changes from extension (–17 %) in "cube-on-cube" to compression (+17 %) in "90 ˚ rotation". In the "83˚ rotation" case, which is quite interesting, the misfit of one set of (111) planes is reduced to - 0.3 %, while the misfit of the other set of (111) planes is as high as 56.7 %. Therefore, the lattice misfit could not be the determining factor for these rotational orientations to occur.

There was no noticeable deposition temperature dependence of the appearance of these rotational oriented islands, at least in the range of our investigation. However, it was found that the interface between a rotational grown nickel island and its underneath titanium nitride is relatively rougher than that for "cube-on-cube" oriented islands. Besides, the rotational epitaxial growth tends to occur in the samples where silicon substrate cleaning was not efficient or in the multilayered samples where epitaxy quality of the template deteriorated as more and more layers of nickel islands are embedded. These facts suggest that the local structure in the template surface plays an important role. It is well known that surface kinetics plays an important role in epitaxial growth. The actual growth dynamics depends on several competing kinetic processes such as adsorption, diffusion, nucleation, chemical bonding, and evaporation, etc. The local atomic configuration (topographical features) of the template surface could directly affect the nucleation site, the mobility of the adatoms, as well as the interfacial inter-atomic bonding length, and hence the bonding energy. Therefore, it is possible that a local thermodynamic equilibrium was reached at certain places when islands growth took the rotational orientation.

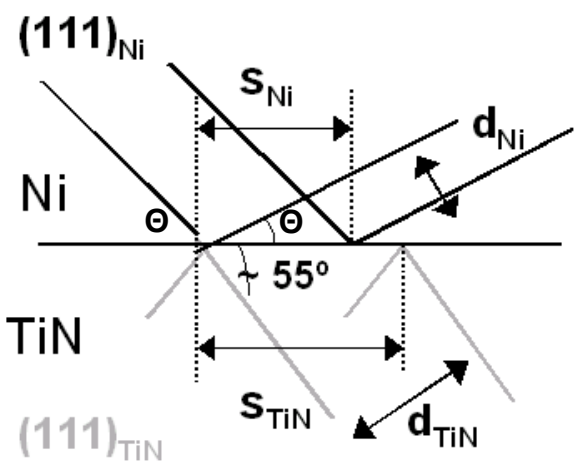

$$misfit = \frac{s_{Ni} - s_{TiN}}{s_{TiN}}$$

$$d_{TiN(111)} = 0.424/\sqrt{3} = 0.245nm$$

$$d_{Ni(111)} = 0.352/\sqrt{3} = 0.203nm$$

$$s_{TiN(111)} = d_{TiN(111)}/\sin 55° = 0.299nm$$

$$s_{Ni} = d_{Ni(111)}/\sin\theta$$

Figure 4-10 Schematic of misfit calculations in nickel epitaxial growth on titanium nitride

Table 4-3 Misfit calculated by considering (111) plane matching at the interface, as shown schematically in Fig. 4-10

Orientation	Inclination Angle θ	s_{Ni} (111)	Misfit
cube-on-cube	~ 55 ˚	0.248 nm	-17 %
~ 90˚ rotation	~ 35 ˚	0.349 nm	17 %
~ 83˚ rotation	~ 28 ˚	0.433 nm	56.7 %
	~ 43 ˚	0.298 nm	- 0.3 %

4.3 ISLAND SHAPE AND FACETING

The equilibrium shape of crystals is the shape that minimizes the total surface energy. Wulf theorem gives the equilibrium shape of a free crystal: the envelope of the planes, which are perpendicular to the direction n and at a distance proportional to the corresponding surface energy γ (n) from a central point (Wulf point) [8]. For crystals grown on a substrate, further modifications have been developed. First, for a structure-less substrate the interfacial energy takes a part, and there is also a truncation of the equilibrium shape [8]. Furthermore, if the crystal is epitaxially grown, the strain energy due to the elastic relaxation also modifies the equilibrium shape [8-10].

The crystals grown by vapor deposition do not always have equilibrium shapes, especially if the deposition was conducted under the pressure far from equilibrium [11]. The growth shape could be affected by many kinetically limiting factors. For examples, the slowest growing faces tend to bound the entire crystal, and also the mobility and stability of small clusters that nucleated on different faces differ from each other.

In this work, although the nickel islands were grown by pulsed laser deposition, which is a non-equilibrium process, it is still reasonable to consider these islands having a close-to-equilibrium shape. The reasons are as follows: (1) the deposition was carried out at elevated temperatures (400 °C to 650 °C), and (2) after deposition, the samples were cooled very slowly to the room temperature, or to ~ 300 ˚C for capping, a process equivalent to annealing to some degree. Finally, the adsorbate impurity induced faceting effect could be neglected since under the deposition vacuum (10^{-6} Torr), the gaseous impurities impingement rate is

approximately 10^{14} molecules/ cm^2-s, which is five orders of magnitude lower than the estimated peak deposition flux of 10^{19} atoms/cm^2-s [12]. This close-to-equilibrium shape assumption is in fact supported by the experimental observations.

As mentioned earlier in Section 4.1, although the common shape of nickel islands is a truncated pyramid, there were also non-truncated pyramidal shaped islands observed. HRTEM (as shown in Fig. 4-7 and Fig. 4-8) study showed that the shape of an island is closely related to its orientation. The truncated pyramidal shaped islands tend to be cube-on-cube oriented, while those non-truncated shaped were grown via rotational orientation.

The faceting information could also be obtained from HRTEM images. It was found that the cube-on-cube oriented (truncated pyramidal) islands are bounded by planes close to (111) at sides and planes close to (100) at the top. In the case of rotational orientated islands, the bounding lattice planes of the pyramidal shaped islands are also (111) facets. The difference lies in the angles formed by the two facing (111) facets: the angle for cube-on-cube oriented (truncated pyramidal) island is about 70° and that for rotational orientated (pyramidal) islands is 110°, which is schematically shown in Fig. 4-11 (a-c). This was also supported by the result of angle measurements from the TEM low-magnification images, where the inclination angle of the sidewall for truncated pyramidal islands is around 55°, which is close to the calculated theoretical value 54.74°.

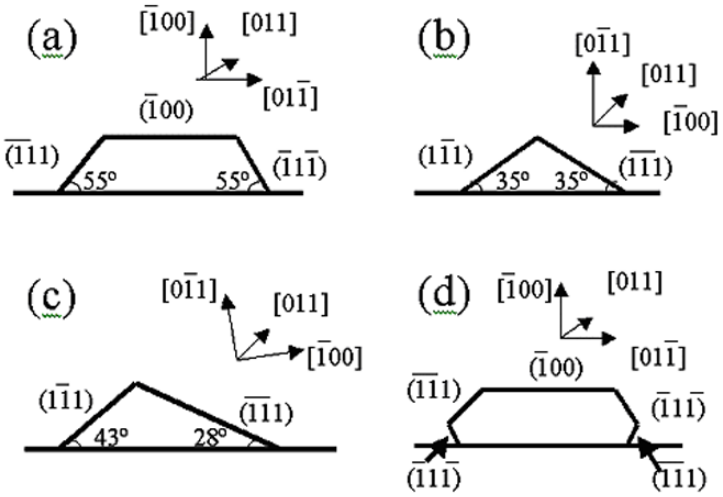

Figure 4-11 Schematic of nickel faceting: (a) a truncated pyramidal shaped island with the "cube-on-cube" orientation; (b) a pyramidal shaped island with rotational orientation (90° rotation); (c) a pyramidal shaped island with rotational orientation (83° rotation) and (d) dewetting phenomenon with the areas exaggerated.

The surface energy data of Ni listed in Table 4-2 is from Vitos and his coworkers' report [4], calculated by ab initio density functional theory (DFT) in generalized gradient approximation (GGA) method. Their results showed that for nickel, (111) facets have the lowest surface energy compared to (100) and (110) facets. For transition metals, the main contribution to the surface energies comes from the dangling bonds at the semi-infinite surface. The number of such bonds increases as the surface becomes more open [4]. Therefore, it is understandable that these islands tend to take the shape, where (111) planes formed a large percentage of the surface (serving as side-walls). Unlike the cube-on-cube oriented islands, the islands grown by rotational orientation do not have a flat top. From the crystallographic point of view, after a close-to-90° rotation, the growth direction of these islands is not the <100> direction anymore. As a result, if there is a "flat-top", it should be the (110) surface

rather than the (100) surface, as shown in Fig. 4-11 (b) and (c). Therefore, we deduce that Ni (110) surface should have higher surface energy than Ni (100) although the theoretical calculations made by Vitos *et al.* [4] shows the opposite (2.368 J cm^{-2} for Ni (110) and 2.426 J cm^{-2} for Ni (100)).

In addition, dewetting has been observed in many cases as schematically shown in Fig. 4-11 (d). From HRTEM images and the angle measurement in low magnification images, it is easily seen that these planes are also (111) planes. This could be explained again by energetics considerations: the energy of the whole system is reduced as a result of replacing some of the high energy interface area by TiN (100) and Ni (111) surface, which are energetically more stable.

The height to lateral size ratio was found to be around 0.3 and no apparent size dependence was observed. The variation of this ratio in the same sample resulted from the lateral size difference rather than the height difference. In fact, in the same sample, the height variation is quite narrow. According to Müller and Kern, who proposed a modified Wulf-Kaishew theorem for Volmer-Weber growth, the epitaxial strain leads to a thickening of the equilibrium shape, and therefore the shape ratio (height over lateral size) of coherent islands is size/volume dependent [8-10]. The entrance of each misfit dislocation will reduce the strain temporally and hence flatten the shape. In the case of nickel growth in this work, the shape ratio loses the size dependence is probably due to the high density of misfit dislocations introduced as a result of a high lattice misfit (17 %).

While cross-sectional TEM study gives a projected island shape along the zone axis direction, plan-view study gives the information on the island base. Fig. 4-12 shows the

plan-view STEM Z-contrast image of nickel islands. It is clearly seen that the island has a rectangular-shaped base. After calibrating the image rotation, it was found that the two principal axes are close to two orthogonal <011> directions. Interestingly, this result closely resembles those obtained in some metal homoepitaxy studies. In the systems such as Cu/Cu (100), Ag/Ag (100) and Fe/Fe (100), the 2D islands formed at the early stage have the similar shape and distribution [14]. This preferred <011> step edge direction is likely to be a result of edge diffusion. At a relatively high deposition temperature, the shape of 2D islands is defined, to a large degree, by those step-edges with lower diffusion barriers since the step-edges with higher energy barrier, and therefore lower migration probability, will advance faster and finally disappear [15]. The diffusion along the densely packed steps is usually faster than along steps with other orientations. Therefore, for growing fcc structured material on (001) surface, the islands will be bounded by (110) step-edges, which are the most close-packed step-edges**.** The kinetic Monte Carlo simulation conducted by Murty and Cooper [16] showed that it is the combined operation of fast edge diffusion and corner diffusion barrier that leads to the step-edge pointing along <110> direction. The interesting point here is that these islands are grown three-dimensionally by domain matching epitaxy, where networks of misfit dislocations are confined to the interface [5-6]. The fact that these (110) edges were still preserved might indicate that the formation of these dislocations did not significantly hinder the atomic diffusion process in the first monolayer, which defines the final island edges. This is reasonable since the energy barrier to form misfit dislocations in heteroepitaxial growth decreases strongly with increase in magnitude of the misfit [1], whereas the misfit is as high as 17% in the Ni/TiN system.

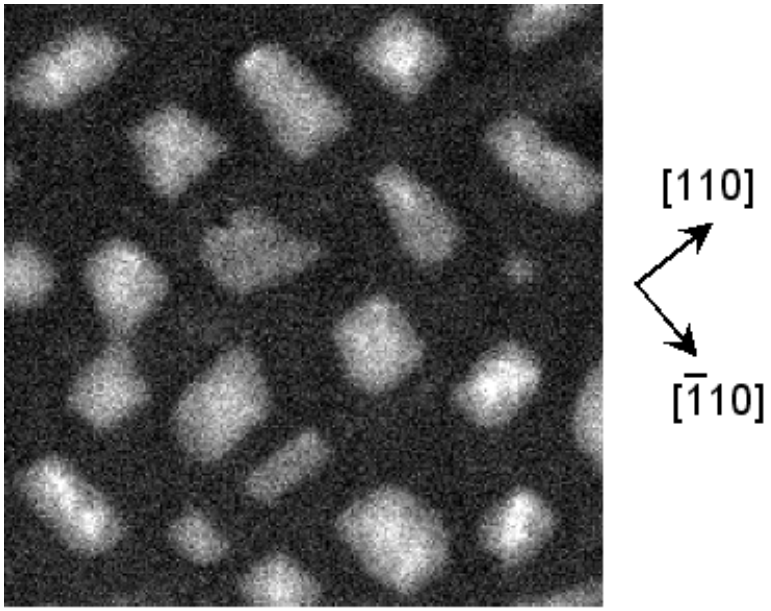

Figure 4-12 A plan-view STEM Z-contrast image of self-assembled Ni islands grown on epitaxial TiN (001) surface. The islands tend to have rectangular bases with two principle axes close to two orthogonal <011> directions.

Combining the results of both cross-sectional and the plan-view TEM study discussed above, we now speculate how an ideal nickel, or probably other fcc metal, islands would epitaxially grow on a (001) surface. The island takes a "cube-on-cube" orientation with a truncated pyramidal shape bounded by four facets close to (111) at sides and (001) facet at the top. The two orthogonal edges of its rectangular/square base are parallel to two <011> directions. This is illustrated schematically in Fig. 4-13 (a). Similarly, the islands grown by "90˚ rotation" could also be deduced: the island takes a nontruncated pyramidal shape bounded by four planes that are close to (111) at sides. It should be noted that even in the rotation case the two orthogonal edges of its rectangular base are still parallel to <011> directions of the substrate (Fig. 4-13 (b)) although for the island itself, one edge has become <100> direction.

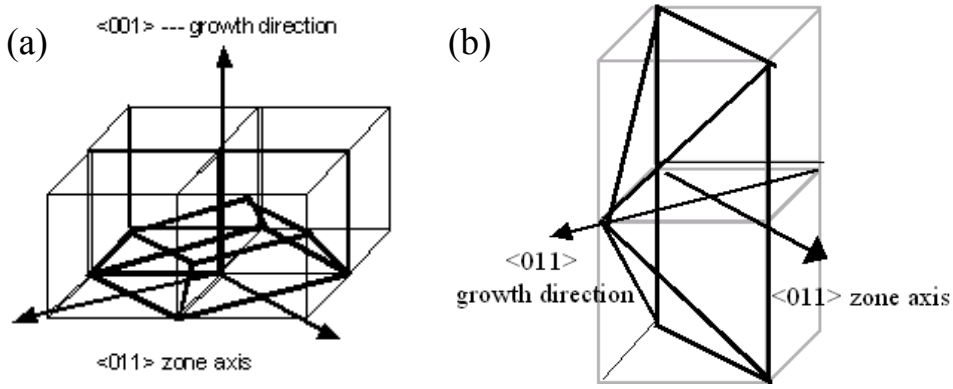

Figure 4-13 Schematic of self-assembled nickel island grown on epitaxial TiN (001) surface: (a) a "cube-on-cube" oriented island takes a truncated pyramidal shape bounded by four facets close to (111) at sides and (001) facet at the top; (b) a "90˚ rotated" island takes a nontruncated pyramidal shape bounded by four facets close to (111) at sides. Note, in both cases, the two orthogonal edges of the rectangular/square base are parallel to <011> directions of the titanium nitride / silicon substrate although in the "90˚ rotation" case for the island itself, one edge has become <100> direction.

References

1. O. Trushin, E. Granato, S. C. Ying, P. Salo, and T. Ala-Nissila, Phys. Rev. B **68**, 155413 (2003)
2. D. J. Eaglesham, A. E. White, L. C. Feldman, N. Moriya, and D. C. Jacobson, Phys. Rev. Letts. **70**, 1643 (1993)
3. M. Marlo, V. Milman, Phys. Rev. B. **62**, 2899 (2000)
4. L. Vitos, A. V. Ruban, H. L. Skriver, and J. Kollár, Surf. Sci. **411**, 186 (1998)
5. J. Narayan, U.S. Patent No. 5, 406, 123 (1995)
6. J. Narayan, and B. C. Larson, J. Appl. Phys., **93**, 278 (2003)
7. F. K. LeGoues, M. C. Reuter, J. Tersoff, M. Hammar, and R. M. Tromp, Phys. Rev. Letts. **73**, 300 (1994)
8. P. Müller, and R. Kern, J. Cryst. Growth, **193**, 257 (1998) and references therein.
9. P Müller, and R. Kern, Surf. Sci., **457**, 229 (2000)
10. P. Müller, and R. Kern, Appl. Surf. Sci., **162**, 163 (2000)
11. J A Venables, G D T Spiller, and M. Hanbucken, Rep. Prog. Phys. **47**, 399 (1984)
12. J J Métois and J C Heyraud, J. Cryst. Growth, **57**, 487 (1982)
13. Gaseous impurities impingement flux $\Phi = 3.513 \times 10^{22} \frac{P}{\sqrt{MT}} molecules/cm^2 - \sec$, where P is the vacuum expressed in Torr, M is the molecule weight of the gaseous impurity, and T is the temperature expressed in K.
14. J. F. Wendelken, Anna K. Swan, Woei-Wu Pai, and J. –K. Zuo, in *Morphological, organization in epitaxial growth and removal*, edited by Z. Zhang and M. Lagally, Series on Directions in Condensed Matter Physics – vol 14, World Scientific Publishing Co, Pte. Ltd, 1998, p320 and references therein.
15. C. Ratsch, P. Ruggerone, and M. Scheffler, in *Morphological, organization in epitaxial growth and removal*, edited by Z. Zhang and M. Lagally, Series on Directions in Condensed Matter Physics – vol 14, World Scientific Publishing Co, Pte. Ltd, , p3. (1998)
16. M.V. Ramana Murty, and B.H. Cooper, Phys. Rev. Lett., **83**, 352 (1999)

5 ISLAND SIZE DISTRIBUTION AND LATERAL ORDERING

5.1 SIZE DISTRIBUTION

Size uniformity is a very important issue for nanostructure fabrication and practical applications. As presented in Chapter 4, the cross-sectional TEM study shows that the lateral size, and especially the height of the formed islands seem quite uniform. However, it is still not possible to draw a firm conclusion about the uniformity since the number of the islands imaged in cross-sectional TEM study was quite limited. Whereas in plan-view study, the image could contain hundreds of islands and therefore it is possible to give a statistical size distribution. Figure 5-1 is a plan-view STEM Z-contrast image of an area containing tens of nickel islands. The histograms shown in Figure 5-2 is a size distribution of islands in terms of base area. Gaussian function fitting showed that the area is 2004 ± 665 nm^2, indicating a relatively narrow size distribution of these islands. It should be noted that some small nickel islands appearing as weak bright dots dispersed among the rectangular-based big islands in the Z-contrast image have not been included in the analysis due to the limitations of the analysis program.

There are basically two stages in the formation of islands by deposition: nucleation and growth. Nucleation occurs first due to the supersaturation of the adatoms, and as a result, the adatom concentration drops. The nuclei then grow by capturing newly deposited adatoms, as well as those detached from neighboring smaller islands due to the Gibbs-Thomson effect, the latter process is called Ostwald Ripening. The observed narrow size distribution indicates that the ripening process has not been fully developed. The tendency for island size

equalization has been reported for many self-assembly systems where islands were coherently grown via S-K (Stranski-Krastanov) mode [1-2]. The kinetic theories state that the ripening could be kinetically slowed down once the islands reach a certain size. The main kinetic limiting mechanism suggested so far is that the strain accumulated in the system, which is proportional to the island size, enhances the energy barrier for the atoms to be incorporated at the island edge [1,3] and also biases the atom diffusion around the island [4]. In the case of nickel epitaxial growth on titanium nitride surface, where the islands were grown by domain matching epitaxy via Volmer-Weber mode, the possibility that the similar mechanisms were operating could not be excluded since even if the introduction of dislocations completely relaxes the system, there is still a strain field in the substrate due to the surface stress discontinuity at the island edges [2,5-6].

Another source of adatoms for island lateral expansion is the atoms jumping from the upper layer, but then there are Ehrlich-Schwoebel step barrier [7-8] and step-adatom interaction [9], and both of them hinder the adatoms hopping from a terrace to the layer below. Brunev ***et al.*** [10] introduced Schwoebel barrier [8] for explanation of three-dimensional growth kinetics. According to their simulation, the atomic upward flux to downward flux ratio has an island size dependence and hence results in island size equalization.

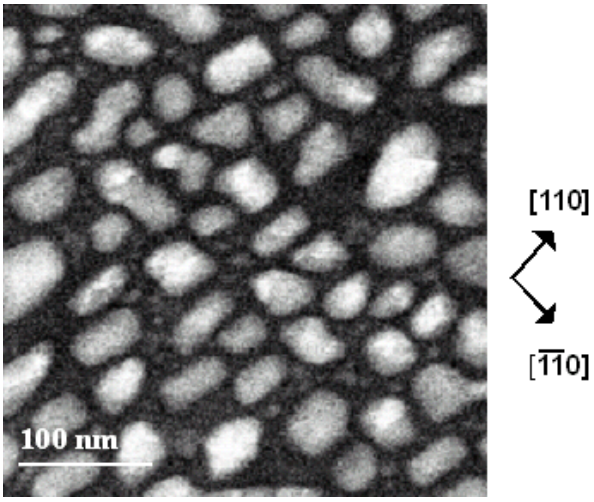

Figure 5-1 A plan-view STEM Z-contrast image of self-assembled Ni islands grown on epitaxial TiN (001) surface. The islands tend to have rectangular bases with two principle axes close to two orthogonal <011> directions and align themselves along the edge directions.

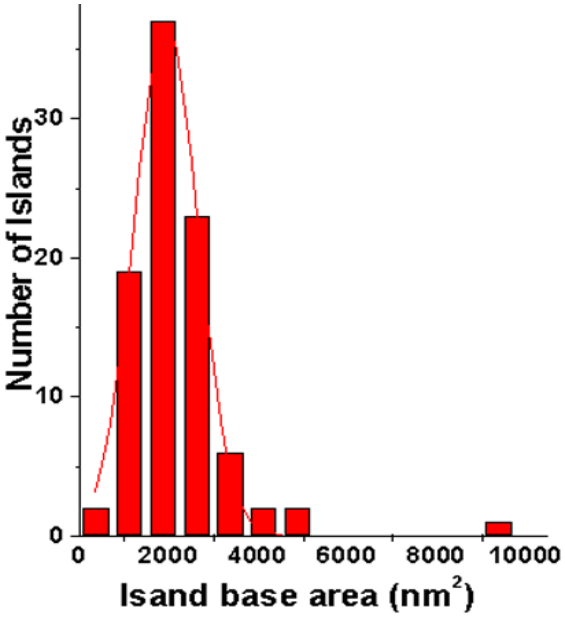

Figure 5-2 Size distribution in term of base area of self-assembled Ni islands grown on TiN (001) surface. The curves are Gaussian distributions.

Fig. 5-3 shows a distribution of island separation between neighboring islands with parallel edges, we can see that there is preferred island spacing, around 17 nm. This suggests that the interaction between neighboring islands very likely plays a more critical role in the size uniformity. As they grow larger and get closer, neighboring islands could interact with each other through the strain field they induced. The overlapping of the strain field between neighboring islands could make the atoms even harder to be incorporated at the island edges. As a result, the ripening is suppressed after the islands reach a certain size. This island-induced strain field interaction could have also helped to maintain the parallel edges of the islands.

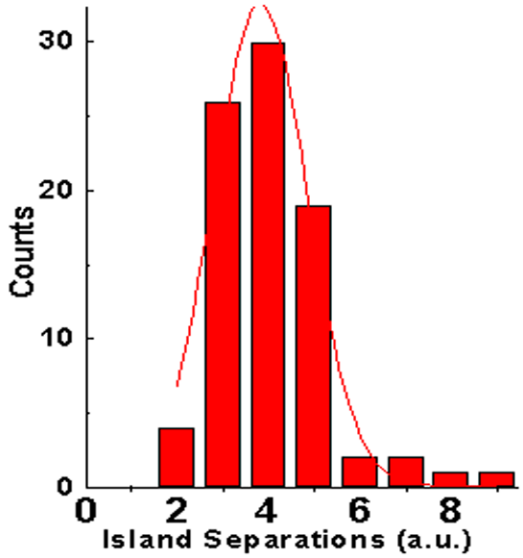

Figure 5-3 Distributions of island separation between the neighboring self-assembled nickel islands with parallel edges. The curves are Gaussian distributions.

Finally, the characteristics of pulsed laser deposition could also have contributed to the size uniformity. The highly saturated plume in PLD leads to a smaller critical nuclei size, and therefore a higher nucleation rate and a higher nuclei density. It is possible that for the first a few pulses, nucleation took place everywhere on the substrate, both heterogeneously and homogeneously. Since these nuclei were formed almost at the same time they are likely to possess a similar capability to attract and trap newly arriving adatoms. As a result, these nuclei will tend to grow into similar size, and therefore sufficient condition for Ostwald Ripening is not established.

All the results presented earlier were obtained from samples where nickel deposition time was controlled around 30 ~ 45 seconds. In other words, the deposition was terminated at relative early stages. It was interesting to carry out a deposition that lasted for longer time. The three images shown in Fig. 5-4 were taken from a sample, where nickel was deposited for 3 minutes at 700˚C. It is obvious that the kind of uniformity in both shape and size seen before is lost, indicating a fully developed Ostwald Ripening. This result suggests that Ostwald Ripening was just temporally suppressed for the samples where the deposition was terminated at an early stage.

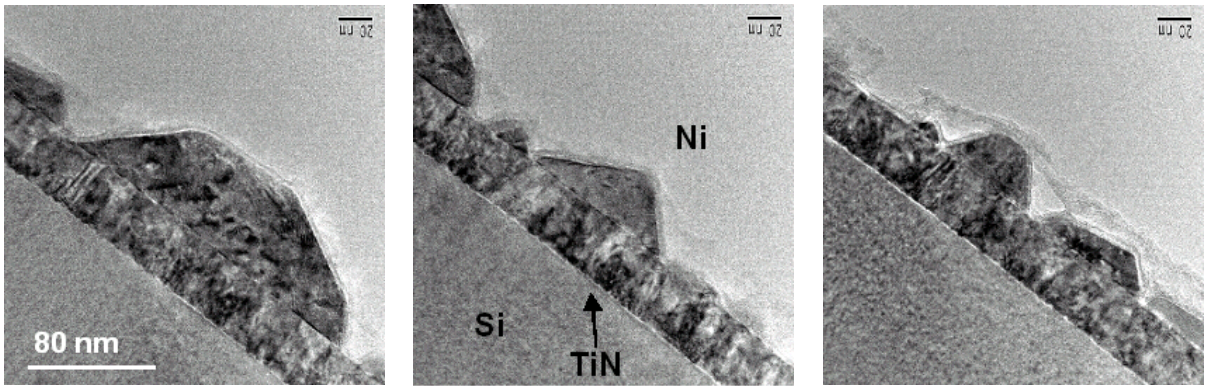

Figure 5-4 Images of nickel islands that were deposited for 3 minutes at 700˚C, showing that uniformity in both shape and size is lost.

5.2 LATERAL ORDERING

The lateral arrangement of the islands was also studied. It was found that the neighboring islands exhibit a certain degree of correlated arrangement: the islands tend to align themselves along the edge directions as shown in Fig. 5-1. This ordering is even more apparent in Figure 5-5, which shows a plot of the island position in terms of the x and y coordinates of the island base center. Obviously, the islands were not completely randomly distributed; some islands chains were formed along the directions close to <011>.

The similar lateral correlation of self-assembled islands grown by S-K growth mode has been reported in many cases [2,6,11-12]. Both theoretical analysis and experimental observations show that the islands should be and indeed aligned along the elastic soft direction, which is <001> in most semiconductor systems being studied [6,11-12]. This was often explained by the elastic interaction between neighboring islands through the substrate/wetting layer in a dense system of islands [6,11-12]. In the case of nickel grown on titanium nitride, it is hard to determine if exactly the same mechanism is operating. Line-focus acoustic microscopy measurements showed that the epitaxial TiN grown on (001) MgO substrate by the ultrahigh vacuum reactive sputtering technique had Young's modulus values of 556, 446 and 418 GPa for [100], [110] and [111] direction, respectively [13]. However, it had been reported that the strain in epitaxially grown films would cause a shift in the elastically soft directions [14]. TiN and MgO both have rocksalt structure with a lattice misfit less than 1% (0.424 nm for TiN and 0.421 nm for MgO), whereas the misfit for TiN grown on Si by domain matching epitaxy depends on the local domain size variation, which could bring the misfit down to zero [15].

However, since the ordering direction is along the edge direction, it is reasonable to conjecture that the interaction of island-induced, or more specifically edge-induced, strain field plays an important role in this lateral ordering. More systematic experiments as well as theoretical studies are needed for further understanding the self-organization behavior of these semi-coherent islands grown via Volmer-Weber growth mode.

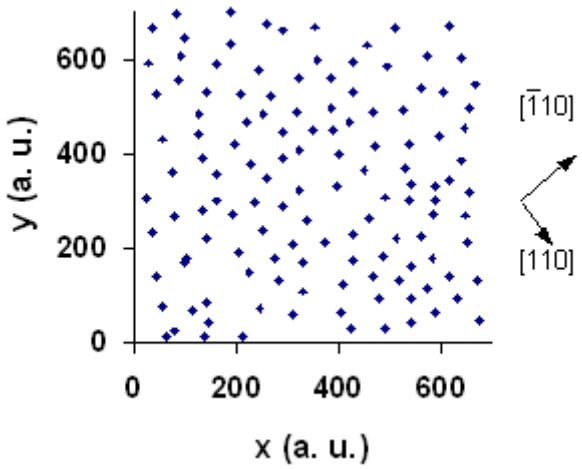

Figure 5-5 A plot of the island positions in terms of the x and y coordinates of the island base center, showing that the islands were not completely randomly distributed: some islands chains were formed along the directions close to <011>.

References

1. N. P. Kobayashi, T. R. Ramachandran, P. Chen, and A. Madhukar, Appl. Phys. Lett. **68**, 3299 (1996).
2. Vitaliy A. Shchukin, and Dieter Bimberg, Rev. Modern Physics, **71**, 1125 (1999), and the references therein.
3. Y. Chen and J. Washburn, Phys. Rev. Lett. **77**, 4046 (1996)
4. Albert-László Barabási, Appl. Phys. Lett. **70**, 2565 (1997)
5. Feng Liu, Phys. Rev. Lett. **89**, 246105 (2002)
6. M. Hanke, H. Raidt, R. Köhler, and H. Wawra, Appl. Phys. Lett. **83**, 4927 (2003)
7. G. Ehrlich and F. Hudda, J. Chem. Phys. **44**, 1039 (1966)
8. Richard L. Schwoebel, J. Appl. Phys., **40**, 614, 1969
9. Jacques G. Amar and Fereydoon Family, Phys. Rev. Lett., **77**, 4584 (1996)
10. D.V. Brunev, I.G. Neizvestny, N.L. Shwartz, and Z. Sh. Yanovitskaya, Phys. Low-Dim. Struct., **11/12**, 325 (2001)
11. M. Meixner, E. Schöll, M. Schmidbauer, H. Raidt, and R. Köhler, Phys. Rev. B **64**, 245307 (2001).
12. K. Zhang, Ch. Heyn, W. Hansen, Th. Schmidt, and J. Falta, Appl. Phys. Lett. **76**, 2229 (2000).
13. J. O. Kim, J. D. Achenbach, P. B. Mirkarimi, M. Shinn, and S. A. Barnett, J. Appl. Phys. **72**, 1805 (1992)
14. V. Ozoliņš, C. Wolverton, and Alex Zunger, Appl. Phys. Lett. **72**, 427 (1998)
15. J. Narayan, and B. C. Larson, J. Appl. Phys., **93**, 278 (2003)

6 MULTILAYERED STRUCTURES

In order to get sufficient signal, all the magnetic measurements were performed on multilayered structures, where layers of nickel islands are separated by titanium nitride or aluminum oxide layers. Here aluminum oxide serves as the template to grow randomly oriented nickel islands, whose magnetic properties were compared with those obtained from crystallographically aligned nickel islands. This chapter presents the structural characterization of these two types of multilayered structures.

6.1 NICKEL / TITANIUM NITRIDE MULTILAYERED STRUCTURES

Understandably, the orientation of nickel islands is determined by the orientation of the underneath titanium nitride, which serves as a template for nickel crystals to grow. In other words, the orientation perfection of nickel islands strongly depends on the epitaxial quality of titanium nitride. In multilayered structures, the epitaxial quality of titanium nitride is expected to deteriorate as more and more layers of nickel islands are embedded. Therefore, investigation on the dependence of orientation perfection of nickel islands on the number of the layers is necessary.

Shown in Figure 6-1 (a) and (b) are the low-magnification image and cross-sectional electron diffraction pattern of a two-layer sample deposited at 600 °C. The diffraction spots contributing from cube-on-cube oriented nickel islands are still clearly seen. Compared with that of the one-layer samples, the diffraction pattern of both nickel and titanium nitride shows obvious signal of texturing: the appearance of arc rather than circular spots indicates that

parts of the crystal were misoriented by a small angle. The rotation of some nickel islands was further confirmed by the X-ray diffraction pattern, as shown in Fig. 6-2. The appearance of a weak Ni (220) peak along with Ni (200), TiN (200) and Si (400) peaks shows that in addition to the majority of "cube-on-cube" oriented islands, there are quite a few islands took the "90˚ rotated" orientation.

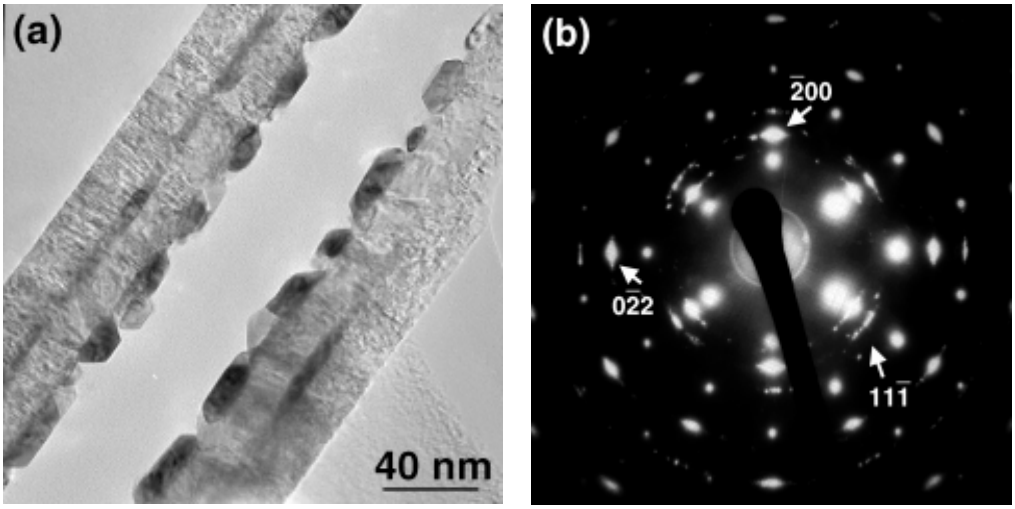

Figure 6-1 (a) Low-magnification image of a sample with two layers of nickel islands; (b) Cross-sectional selected area electron diffraction along Si <011> zone axis of the same sample. The texturing of TiN and Ni is obvious.

Minimizing the interruption to the epitaxy growth of titanium nitride film caused by accommodation of nickel islands is a direct way to improve the orientation perfection of template (titanium nitride) and therefore nickel islands. Fig. 6-3 (a) is a cross-sectional STEM-Z contrast image of a sample of three layers of nickel islands, where the deposition time of nickel was reduced from 40 seconds (used in two-layer sample) to 20 seconds. Fig. 6-3 (b) is the SAD pattern taken from the area containing three layers of nickel and titanium

nitride. It is easily seen that the texturing of titanium nitride has been greatly suppressed. The cube-on-cube nickel spots are weak due to the significant decrease in the amount of nickel, but still visible. Besides, double diffraction spots from titanium nitride and nickel also appeared since the first two layers of nickel are embedded in a titanium nitride matrix. The fact that we can still get a moderate template crystalline quality for multi-layer samples is partially due to the lateral epitaxy of titanium nitride, which originates from the titanium nitride areas uncovered by nickel islands in the previous layer.

Interestingly, the faceting discussed in Chapter 5 is not valid here. The wetting angle in most cases is close to 90˚, which means that the bounding facets could not be (111) planes. There are two possible reasons. First, this might be a growth shape rather then a close-to-equilibrium shape. The nickel islands were covered (capped) by titanium nitride almost immediately after the deposition since the deposition temperature for both materials is 600 ˚C, and therefore no annealing effect got involved. On the other hand, the interfacial energy of Ni/TiN and Ni/vacuum could be very different, and therefore leads to different faceting.

Finally, it should be noted that the interlayer correlation, which was reported in many multi-layered structures with islands grown via S-K mode, was not observed here due to the much thicker spacer layer [1-5].

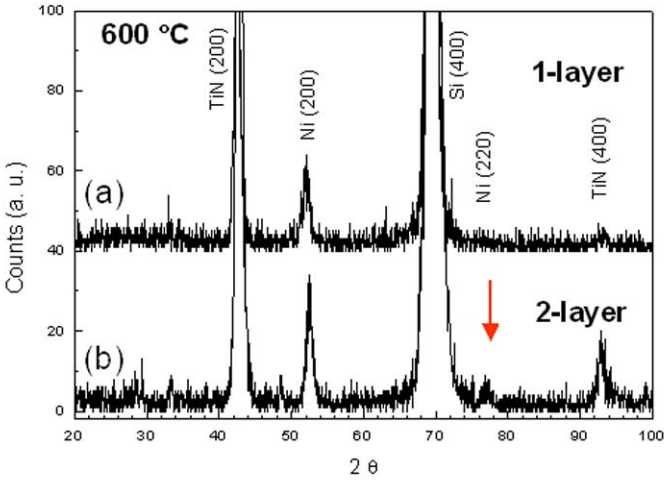

Figure 6-2 X-ray diffraction patterns of samples containing (a) one-layer and (b) two-layer nickel islands grown at 600 ℃. For the two-layer sample, (220) reflection from Ni islands grown via "90˚ rotational orientation" is also seen.

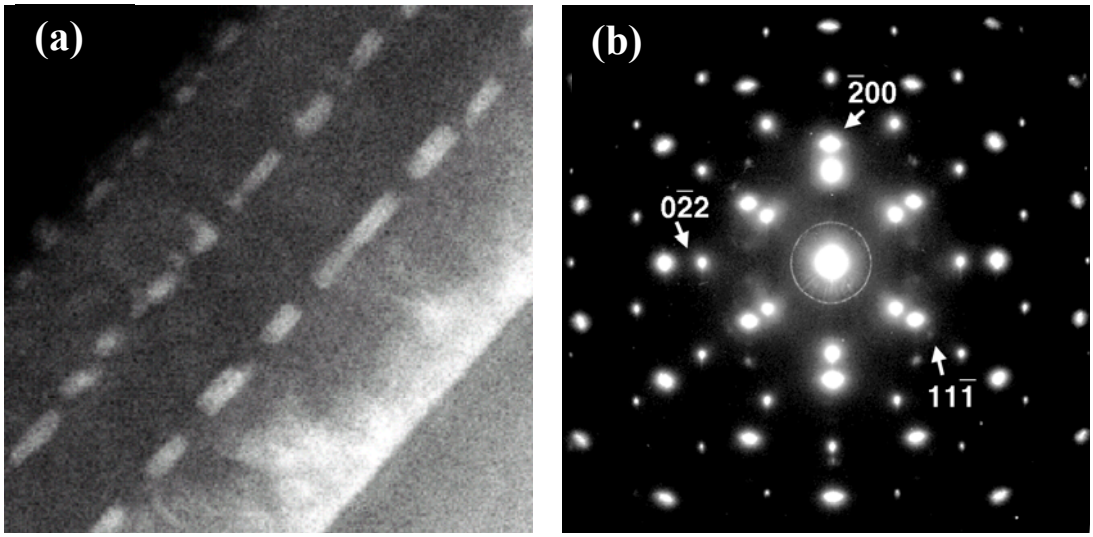

Figure 6-3 (a) A STEM Z-contrast image of a sample with three layers of nickel islands, where the deposition time of nickel is reduced to 20 seconds; (b) Cross-sectional selected area electron diffraction along Si <011> zone axis of the same sample. The texturing of TiN and Ni is significantly suppressed.

6.2 NICKEL / ALUMINUM OXIDE MULTILAYERED STRUCTURES

In order to study the effect of the crystallographic orientation of nickel islands on the magnetic properties, crystallograhpically randomly oriented nickel islands were prepared by using amorphous/polycrystalline aluminum oxide as the template.

Fig. 6-4 is a Si <011> zone axis low magnification TEM image of a sample where nickel islands were grown in aluminum oxide matrix. The deposition temperature of nickel and aluminum was 450 ˚C and 300 ˚C, respectively. The image clearly shows that nickel formed multi-faceted three-dimensional islands with lateral size around 20 nm.

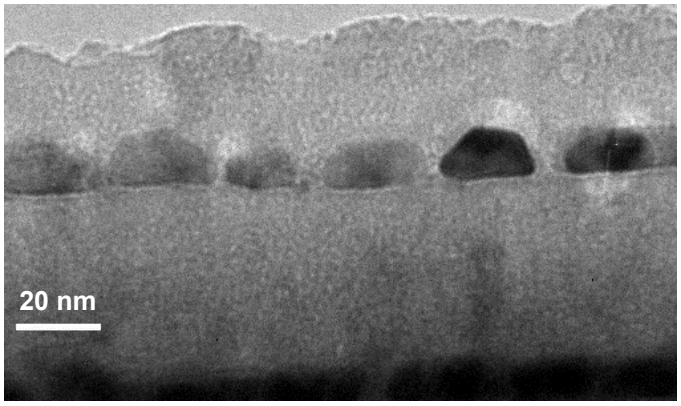

Figure 6-4 A low magnification image of nickel islands grown on aluminum oxide matrix

High resolution TEM study shows that although a number of nickel islands are of single crystal, there are a quite few islands with planar defects, such as grain boundaries and

stacking faults, as the two shown in Fig. 6-5. In addition, it was also seen that the aluminum oxide is polycrystalline rather than amorphous.

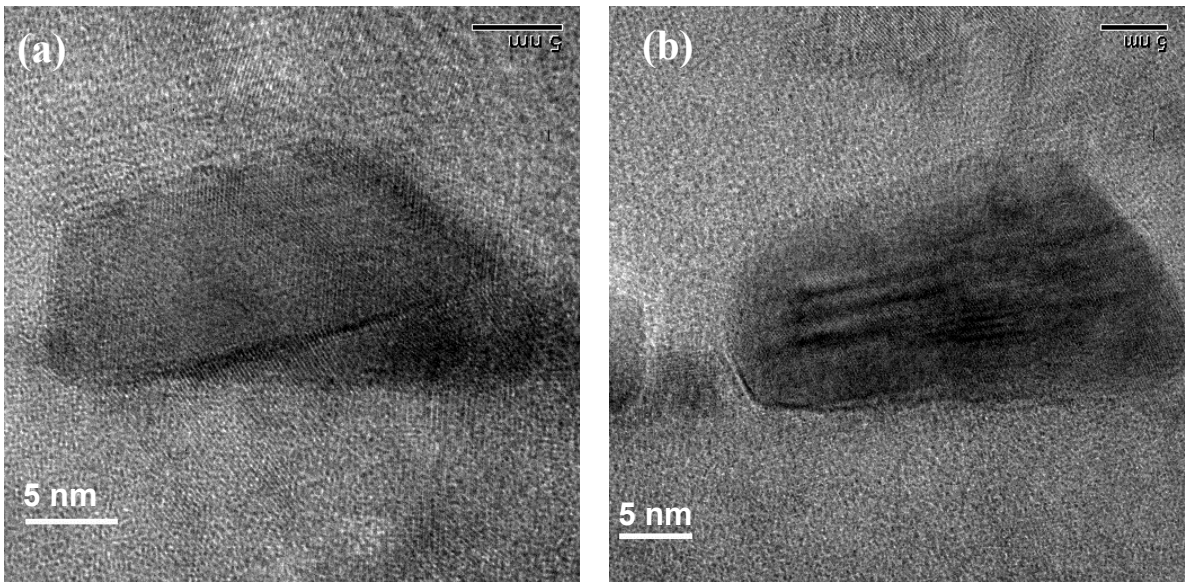

Figure 6-5 HRTEM image of nickel islands embedded in aluminum oxide matrix, the planar defects are clearly seen: (a) a grain boundary, and (b) stacking faults.

REFERENCES

1. Qianghua Xie, Anupam Madhukar, Ping Chen, and Nobuhiko P. Kobayashi, Phys. Rev. Lett., **75**, 2542 (1995)

2. E. Mateeva, and P. Sutter, Appl. Phys. Lett. **71**, 3233 (1997)

3. Vinh Le Thanh, V. Yam, P. Boucaud, Y. Zheng, D. Bouchier, Thin Solid Films, **369**, 45 (2000)

4. G. Spingholz, M. Pinczolits, V. Holy, S. Zerlauth, I. Vavra, G. Bauer, Physica, E **9**, 149 (2001)

5. Vitaliy A. Shchukin, and Dieter Bimberg, Rev. Modern Physics, **71**, 1125 (1999), and the references therein.

7 MAGNETIC PROPERTIES

Magnetic measurements were performed on two systems: multi-layered nickel islands grown in epitaxial titanium nitride matrix and multi-layered nickel islands grown in polycrystalline/amorphous aluminum oxide matrix. As presented in Chapter 6, the crystallographic orientation distribution of nickel islands in these two systems is completely different due to the different crystalline structures of the matrix (template). In Ni/TiN, the islands were epitaxially grown, and therefore their orientations were strongly correlated by the matrix. In an ideal state, they would share the same orientation, which is "cube-on-cube" with respect to the titanium nitride and the silicon (100) substrate. In Ni/Al_2O_3, due to the polycrystalline/amorphous nature of the matrix, this correlation does not exist, and therefore, the crystalline orientations of the nickel islands are randomly dispersed.

Shown in Fig. 7-1 are the ZFC/FC curves for the two systems. There are usually two characteristic temperatures in a ZFC/FC curve: (1) the temperature where ZFC magnetization reaches the maximum, and (2) the temperature where ZFC and FC bifurcates. Ideally, these two temperatures should be the same [1-3]. The difference comes from the blocking temperature distribution, which is the result of the size distribution of magnetic particles. Usually, the peak position in ZFC curve is considered to be the mean blocking temperature, while the difference between the average blocking temperature and the temperature where the bifurcation sets in corresponds to the particle size distribution [4]. According to Fig. 7-1, the blocking temperature is about 30 K and 190 K for Ni/Al_2O_3 and Ni/TiN, respectively, and the ZFC/FC curve bifurcates at 100 K for Ni/Al_2O_3 and 275 K for Ni/TiN system.

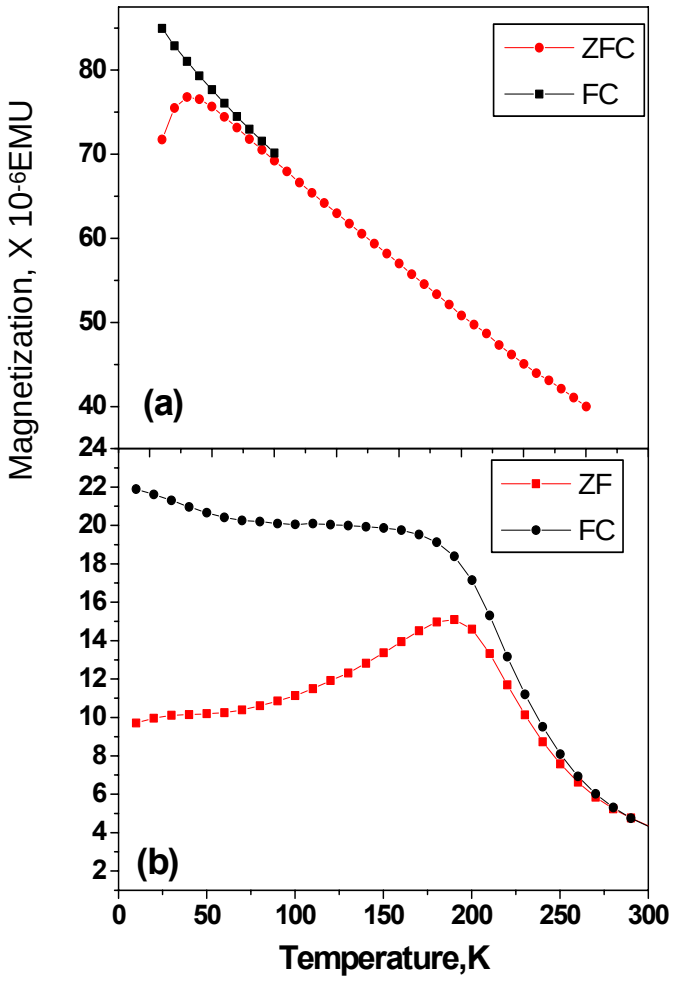

Figure 7-1 ZFC and FC magnetization data as a function of temperature for (a) Ni/Al_2O_3 and (b) Ni/TiN samples

The difference between the two characteristic temperatures, which is 70 K for Ni/Al_2O_3 and 85 K for Ni/TiN, indicates that there exists particle size distribution in both cases. Since the samples used for magnetic measurements are multi-layered samples, the particle size

distribution could result not only from the size variation of the particles on the same layer, but also from the size variation of the particles on different layers. The latter was clearly seen in cross-sectional STEM Z-contrast images of multi-layered samples (e.g. Fig.6-3). Although the deposition time of nickel was kept the same, the size of islands seemed smaller at upper layers. This could be explained by the decrease in deposition rate as a result of the laser-target interaction induced target surface morphology modification. The enhanced blocking temperature in Ni/TiN system will be discussed later in detail.

Fig. 7-2 shows the magnetization versus magnetic field (M~H) curves measured at varied temperatures from 10 K to 300 K for the two systems. It is easily seen that Ni/Al_2O_3 already loses hysteresis behavior at 50 K, whereas Ni/TiN system remains hysteresis behavior till the temperature close to 200 K. This is consistent with the average blocking temperatures of the two systems obtained from ZFC/FC results, which are 50 K and 190 K for Ni/Al_2O_3 and Ni/TiN, respectively. The material behaves ferromagnetically below blocking temperature with high value of coercivity. Above the blocking temperature, the magnetization is unstable and the sample loses any hysteresis responses and exhibit superparamagnetism. In addition, while the two systems are both at ferromagnetic regime, Ni/TiN exhibits higher coercivity (550 Oe) than Ni/Al_2O_3 (150 Oe).

The coercivity as a function of nickel island size (lateral size) measured at different temperatures for Ni/TiN system is shown in Fig. 7-3. Theoretically, there are three regions in a *coercivity vs magnetic particle size* curve: multi-domain region, single domain region, and superparamagnetic region, as discussed in Section 2.1. In multi-domain regime, the coercivity increases as the size decreases and reaches the maximum when entering the single

domain regime. After that the coercivity decreases with the size due to the lowered anisotropy energy barrier for magnetic moments to rotate because it is proportional to the particle volume. As the size further decreases, the superparamagnetism will set in and the particles lose hysteresis behavior, therefore, no coercivity is observed. The monotonic increase in coercivity with particle size shown in Fig. 7-3 indicates that the nickel islands are in the single domain region.

How a system of magnetic particles responds to the magnetic filed is, to a large degree, determined by the effective anisotropy energy barrier, which must be overcome for the particle magnetic moment to rotate. For example, the blocking temperature for magnetic particles with a certain size is determined by the anisotropy energy barrier through Eq. 2.5, and the anisotropy energy also sets the theoretical upper limit for coercivity according to Stone-Wohlfarth mode [5]. Therefore, in the following, the different behavior of Ni/TiN and Ni/Al_2O_3 will be discussed in the light of the anisotropy energy barrier of the two systems.

Blocking temperature is the temperature where the superparamagnetism sets in. The magnetic particles become unblocked only when the thermal energy is sufficient to compete with the anisotropy energy barrier to cause the magnetic moment to fluctuate between different easy magnetization directions. The superparamagnetic relaxation time τ follows the Eq. 2.5-b given in Section 2.1.2:

$$\tau = \tau_0 \exp(E_B / k_B T)) \qquad (7.1/2.5\text{-b})$$

where τ_o is related to the natural frequency of gyromagnetic precession, which is normally taken to be ~10^{-9} seconds. E_B is the anisotropy energy barrier and k_BT is the thermal energy with k_B the Boltzmann constant and T the temperature.

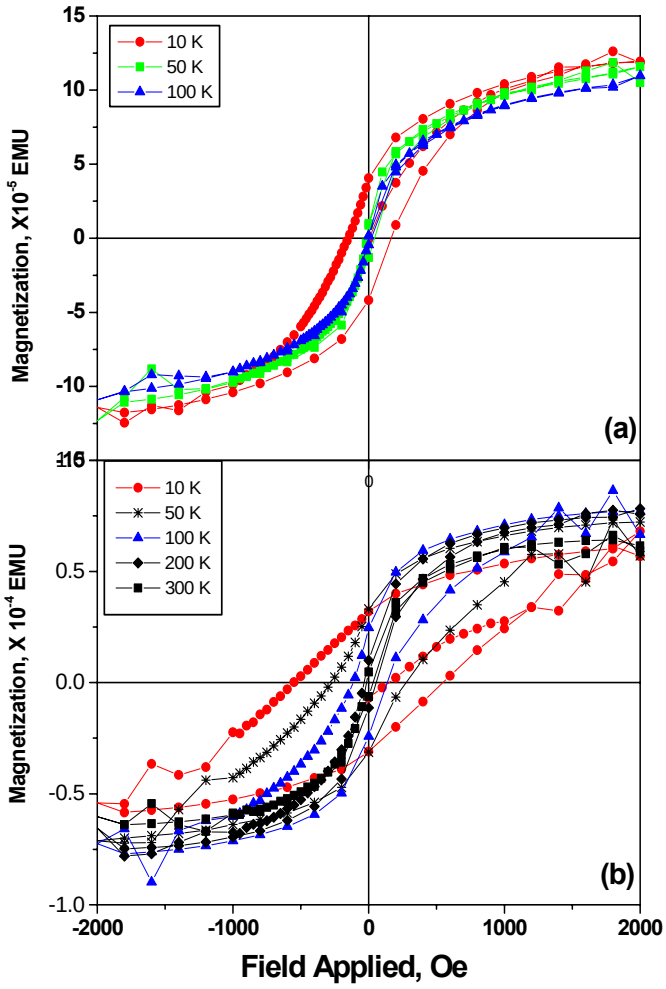

Figure 7-2 Magnetization versus field (M~H) curves for (a) Ni/Al_2O_3 and (b) Ni/TiN samples. The lateral size of islands is around 20 nm.

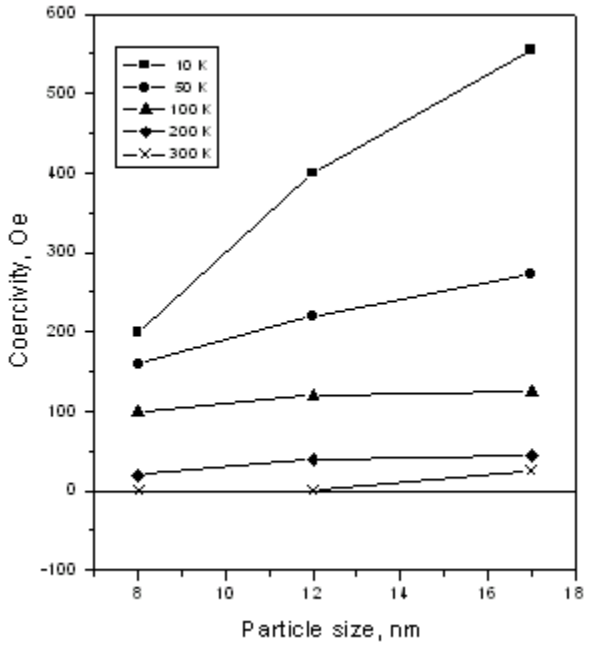

Figure 7-3 Coercivity as a function of particle size at different temperatures for Ni/TiN system

As discussed in Section 2.1.2, the blocking temperature measured is directly related to the characteristic measurement time τ_i by [6]

$$T_{Bi} = \frac{E_B}{k_B[\ln(\tau_i / \tau_0)]} \qquad (7.2/2.6)$$

Since in this work, the characteristic measurement time is 100 seconds, the criterion of blocking temperature is

$$E_B = 25\ k_B T \qquad (7.3)$$

For small magnetic particles the anisotropy barrier could have several contributions as discussed in Section 2.1.3, such as magnetocrystalline, shape, surface/interface, stress, and interactions.

The value of magnetocrystalline anisotropy constant K_1 for Ni at low temperatures is ~ - 7.5 × 10^5 ergs/cm^3 [7]. For cubic anisotropy with minus K_1, the anisotropy energy barrier is [8-9]

$$E_B = \frac{1}{12}|K_1|V \tag{7.4}$$

If we assume all the particles (islands) are of plate-like shape with a square base, then according to the lateral size and height determined by the cross-sectional TEM images, the volume of each particle is 18 nm × 18 nm × 9 nm = 2916 nm^3. Then based on Eq. 7.3 and 7.4, one can calculate the blocking temperature that resulted from the magnetocrystalline anisotropy is 52.8 K.

This value is close to the average blocking temperature obtained in Ni/Al_2O_3 system, which is 30 K. If taking into account the overestimation that could have been involved in the volume calculation, such as using plate-like shape rather than pyramidal shape, and a square base rather than a circular base, it is reasonable to conclude that the magnetocrystalline energy barrier alone could have caused the particle blocking in Ni/Al_2O_3 system.

In contrast, the blocking temperature in Ni/TiN system, obviously, could not be explained by magnetocrystalline anisotropy. Following the same calculation based on Eq. 7.3 and 7.4, one could see that to reach a blocking temperature of 190 K, for the same particle volume,

the magnetocrystalline anisotropy constant K_1 has to be as high as 2.7×10^6 ergs/cm^3. Therefore, there must be contributions from sources other than magnetocrystalline anisotropy that play a critical role in the magnetic reversal process.

For uniaxial anisotropy, the anisotropy energy barrier is

$$E_B = KV \tag{7.5}$$

where K is the anisotropy energy per unit volume, which is also called anisotropy energy constant. Similarly, combining Eq. 7.3 with Eq. 7.5, one can calculate the effective uniaxial anisotropy energy per unit volume that leads to a blocking temperature of 190 K to be 2.3×10^5 ergs/cm^3, or 2.3×10^4 J/m^3.

Shape anisotropy could be a possible contributor since in both systems, the island shape is not spherical. According to Eq. 2-9, a nickel particle in oblate spheroid shape with axis ratio c/a (lateral size to height) equals to 2 does have a shape anisotropy energy constant of 4.2×10^5 ergs/cm^3. However, the fact that the c/a ratios in the two systems are close to each other makes the shape anisotropy not likely the determining factor.

Another source that has possibly contributed to the effective anisotropy barrier difference is the stress. Unlike in Ni/Al_2O_3 system, the nickel islands in Ni/TiN system were epitaxially grown inside TiN, and therefore due to the lattice misfit there exists surface stress. According to Eq. 2-10, the anisotropy energy barrier induced by stress is

$$K = \frac{3}{2}\lambda\sigma = \frac{3}{2}\lambda E\varepsilon \tag{7.6}$$

where ε is the strain which is related to stress σ via the elastic modulus E by σ = E ε [10]. The strain in an epitaxial system strongly depends on whether the interface is coherent or incoherent. The induced anisotropy drops abruptly when the interface changes from coherent, where it is a volume anisotropy, to incoherent, where it is a surface anisotropy. Obviously, the interface between nickel and titanium nitride matrix is incoherent, or semicoherent, due to the existence of the network misfit dislocations. den Broeder *et al.* [11] gave a simple expression of the contribution to the anisotropy from an incoherent interface with dislocations

$$K = \frac{3}{4}\lambda Gb \tag{7.7}$$

where G is the shear modulus and the b is the Burgers vector of the dislocations. λ slightly depends on the crystal directions. Here 2×10^{-5}, a value typical for many materials, is taken, and G for nickel is 80 GPa, b is $\frac{a}{2}\langle 110\rangle$ with *a* the lattice constant of nickel, then K equals to 0.3 mJ/m^2. Obviously, this strain induced surface anisotropy is negligible compared to 2.3×10^4 J/m^3, the value of volume anisotropy needed to result in a blocking temperature of 190 K.

The behavior of a magnetic particle in a magnetic field is not only governed by its own intrinsic anisotropy energy, but also by the coupling with its neighbors. The interplay between the two could modify the magnetic responses of the particles. Therefore, the effective anisotropy energy extracted from the experiments could include two parts: the

intrinsic anisotropy of individual particles and the additional anisotropy induced by the particle interaction.

Each single domain ferromagnetic or ferrimagnetic particle as a whole has an associated net magnetic moment. If the two particles are in close proximity, then the magnetostatic interaction (dipolar interaction) is unavoidable. It has been studied intensively either by simulations or experiments on how the magnetostatic interactions affect the magnetic behavior of a particle system, e.g. whether they decelerate or accelerate the relaxation process. Many results show that there is an increase in the local energy barrier due to the interaction effect, i.e., they lead to an additional anisotropy energy [12-16]. However, there are also different results. For example, a lowered anisotropy energy barrier [17], or a shift toward higher barrier only for low anisotropy [18-19]. In addition, there are also results that could not be simply explained by an increase in the anisotropy energy barrier. Mørup proposed a "superferromagnetic" ordering arising from the particle interaction [20].

Dipolar interaction exists, irrespective of the matrix. However, its modifying effect should not be the determining factor that leads to the different magnetic behavior of nickel islands in the two systems. First, the dipolar anisotropy energy constant has a strong dependence on the particle separation, e.g. $1/r^3$ dependence of the particle separation with r the center-to-center particle distance [12]. Therefore, the dipolar interaction induced anisotropy in both Ni/TiN and Ni/Al_2O_3 system should be small since the particle separation is of tens of nanometers. Second, the particle separations in the two systems are not far different from each other.

Systems that contain regular array of magnetic elements have attracted extensive interest since they are possible candidates for applications such as high-density storage media [21] and magnetoelectronic devices [22-23]. The difference between the magnetic behavior of a system with randomly distributed magnetic elements and a system with regularly positioned magnetic elements mainly lies in the enhanced collective effects. For example, due to the anisotropic nature of the dipolar interaction, the self-organization of magnetic elements would lead to an enhanced dipolar interaction and therefore, collective magnetic properties. This collective effect could produce long-range order in the orientation of the particle magnetic moments, either ferromagnetic or antiferromagnetic depending on the lattice symmetry [24-25].

As presented in Section 5.2, nickel islands in titanium nitride matrix have a rectangular base and exhibit certain degree of ordering along <011> direction, which is also the step-edge direction. Although this is far from a regular 2-D lattice, the local ordering and symmetry still could have enhanced the particle interaction and therefore led to collective properties [26-27], which manifested themselves in the elevated blocking temperature.

The self-organization of the nickel islands in Ni/TiN could also have induced the higher coercivity of the system. It was found that the orientation of the edge and the corner of the magnets are very susceptible to external applied fields and their relative orientation to the field determines the initiation of the reversal mechanisms in the array [26]. In Ni/TiN, the field is applied along one of the in-plane <110> directions, which means that the field direction is parallel or at least close to parallel to one of the island step-edges. While in Ni/Al_2O_3, there is no fixed orientation relationship between the island edges and the external magnetic field. In addition, the existence of the alignment of easy axis in some nickel islands

in Ni/TiN system could also have contributed to the higher coercivity. As discussed earlier in this chapter, due to the far-from-spherical shape of nickel islands in both systems, the shape anisotropy should not be neglected. Since in both systems, the lateral size to height ratio nearly equals to two, the easy directions should be in the plane. Most nickel islands in Ni/TiN have a rectangular base, resulting in an easy direction along the long axis of the rectangle. Therefore, the kind of self-organization of the nickel particles in the TiN matrix could lead to a certain degree of alignment of the easy axis. The introduction of an aligned anisotropy distribution could alter the particle interaction and reversal process significantly. According to the investigation conducted by Ridley *et al.*, the alignment of uniaxial anisotropy leads to a highly symmetric cooperative switching mechanism [28].

The different nature of the matrix could not be ignored, either. Ni/Al_2O_3 is an insulator and the only possible particle interaction is magnetostatic interaction, whereas in Ni/TiN, apart from the magnetostatic interaction, the particles could also possibly be exchange coupled through the conducting TiN matrix. This kind of indirect exchange coupling has been studied intensively in layered systems. The coupling strength is found to be a decreasing function of the spacer thickness and the coupling nature is oscillatory depending on the spacer thickness, which is similar to the well-known Ruderman-Kittel-Kasuya-Yoshida (RKKY) phenomenon, but with a longer oscillatory period (~ 1 nm). In the quantum mechanical approach, this effect is explained by the spin dependent reflectivity of electrons at the nonmagnetic/magnetic interfaces. The interference effects between different reflectivities lead to stabilization of ferromagnetic alignment for certain values of the interlayer thickness and antiferromagnetic alignment for others [29]. The exchange coupling strength could be strongly diminished by the electron scattering caused by the structural

imperfections. Considering the dislocations distributed on the interface and the more than 10 nanometer's particle separation, it is reasonable to conclude that the exchange coupling, if any, will not strongly affect the magnetic reversal process in the Ni/TiN system.

In summary, the enhanced ferromagnetic properties of the nickel islands embedded in epitaxial titanium nitride matrix comes from their self-assembled nature, which alignes the magnetocrystlline anisotropy of the particles, and the self-organized nature, which enhances the particle interaction and leads to more symmetric reversal in a more coherent way.

REFERENCES

1. W. Luo, S. R. Nagel, T. F. Rosenbaum, and R. E. Rosensweig, Phys. Rev. Lett. **67**, 2721 (1991)
2. R. W. Chantrell, N. S. Walmsey, J. Gore, and M. Maylin, Appl. Phys. Lett. **85**, 4320 (1999)
3. B. D. Cullity, Introduction to Magnetic Materials (Addison–Wesley, Reading, MA, 1972)
4. J. C. Denardi, A. L. Brandl, M. Knobel, P. Panissod, A. B. Pakhomov, H. Liu, and X. X. Zhang , Phy. Rev. B **65**, 064422 (2002)
5. R C Stoner, and E. P. Wohlfarth, Philos. Trans. R. Soc. London, Ser. A **240**, 599 (1948)
6. C. L Chien, NanoStructured Materials, **1**, 179 (1992)
7. R. M. Bozorth, Ferromagnetism, Van Nostrand, Princeton, N.J., p. 569 (1951)
8. I. S. Jacobs and C. P. Bean, *Magnetism*, edited by G. T. Rado and H. Suhl (Academic, New York, (1963), Vol. III, pp. 271-294
9. B. P. Bean and J. D. Livingston, J. Appl. Phys. **30**, 120S (1959)
10. M. T. Johnson, P J H Bloemen, and F J A den Broeder, and J J de Vries, Rep. Prog. Phys. **59**, 1409 (1996)
11. F. J. A. den Broeder, W. Hoving, and P.J.H Bloemen, J. Magn. Magn. Mater., **93**, 562 (1991)
12. S. Mørup, J A Dumesic, and H Topsøe, in *Applications of Mössbauer Spectroscopy*, edited by R. L. Cohen (Academic, New York, 1980), Vol. 2, Chap. 1
13. J. L. Dormann, D. Fiorani, and E. Tronc, Adv. Chem. Phys. **98**, 283 (1997)
14. J. L. Dormann, L. Bessais, and D. Fiorani, J. Phys. C **21**, 2015 (1988)
15. C. Petit, A. Taleb, and M. P. Pileni, J. Phys. Chem. B., **103**, 1805 (1999)
16. D. Kechrakos, and K. N. Trohidou, Appl. Phys. Lett. **81**, 4574 (2002)
17. E. Z. Meĭlikhov and R. M. Farzetdinova, Journal of Experimetnal and Theoretical Physics, **98**, 1198 (2004)
18. Verdes, C, Ruiz-Diaz, B, Thompson, S H, Chantrell, R W, and Stancu, Al, 2002, Phys. Rev. B, **65**, 174417
19. Dmitri V. Berkov, IEEE Trans. Magn., **38**, 2637 (2002)

20. Steen Mørup and Gunnar Christiansen, J. Appl. Phys., **73**, 6955 (1993)

21. *The Physics of Ultra-High-Density Magnetic Recording*, edited by M.L. Plumer, J. van Ek, and D. Weller (Springer, Berlin, 2001).

22. G. Prinz, Science **282**, 1660 (1998)

23. S.A. Wolf, D.D. Awschalom, R.A. Buhrman, J.M. Daughton, S. von Molnar, M.L. Roukes, A.Y. Chtchelkanova, and D.M. Treger, Science **294**, 1488 (2001)

24. A A Fraerman, S A Guesev, I M Nefedov, Yu N Noztrin, I R Karetnikova, L A Mazo, M V Sapozhnikov, I A Shereshevsky, and L V Suhodoev, J. Phys: Condens. Matter **13**, 683 (2001)

25. Paolo Politi, and Maria Gloria Pini, Phys. Rev. B, **66**, 214414 (2002)

26. R. L. Stamps, and R E. Camley, Phys. Rev. B, **60**, 11694 (1999)

27. J. Legrand, C. Petit, Appl. Surf. Sci. **164**, 186 (2000)

28. P. H. W. Ridley, G. W. Roberts, and R. W. Chantrell, J. Appl. Phys., **92**, 1069 (2002)

29. P.A. Grünberg, Sensors and Actuators, A **91**, 153 (2001)

8 CONCLUDING REMARKS

Volmer-Weber (V-W) epitaxial growth has been investigated as a potential candidate to fabricate crystallographically orientated magnetic nanostructures. Nickel was deposited on epitaxial titanium nitride (001) surface by pulsed laser deposition (PLD) technique. The structural characterizations include X-ray diffraction (XRD) and both cross-sectional and plan-view transmission electron microscopy, such as SAD, CTEM, HRTEM, and STEM Z-contrast imaging. Magnetic measurements were conducted by superconducting quantum interference device (SQUID) magnetometer and the results were compared with that obtained from the ensemble of randomly oriented nickel islands, which are grown on polycrystalline/amorphous aluminum oxide matrix layer.

It was found that the growth of nickel on titanium nitride (001) surface is three-dimensional epitaxial in accordance with V-W mode. Furthermore, as long as the deposition is terminated at early stages, the formed islands exhibit self-assembled natures, i.e., a certain degree of uniformity in orientation, shape, and size. Under the optimized conditions, the orientation relationship is Ni {100} // TiN {100} // Si {100}, the so-called “cube-on-cube” relationship. The islands are faceted with truncated pyramidal shapes, bounded by planes that are close to (111) at sides and (100) at the top. The base of islands is rectangular with the two principal edges parallel to two orthogonal <011> directions. The actual size of islands varies from a few nanometers to tens of nanometers, depending on the deposition time chosen. The size distribution is relatively narrow; comparable to that obtained from self-assembled islands grown under Stranski-Krastanov (S-K) mode. A certain degree of self-organization was also found in the island lateral distribution: island chains were observed along the directions close

to <011>, which are also the edge directions. The truncated pyramidal shape with (111) and (001) facets was considered to be thermal dynamically stable, which was supported by the surface energy data. Both the size uniformity and the lateral ordering are believed to be strongly related to the interaction between neighboring islands through the stain field induced by island edges.

Other orientations for nickel island growth have been also observed in some samples. In most cases, the (111) planes of nickel crystallites tilted themselves about a certain angle toward the TiN/Ni interface. These rotational orientations did not bring a lattice misfit reduction and their appearance did not show any deposition temperature dependence. However, the appearance of these rotational orientations seem to be closely related to the crystalline quality of titanium nitride template, which suggest that the local structure of the template, in terms of atomic configuration and topographical feature, is responsible for this rotational orientation.

The shape of an island is orientation dependent. The truncated pyramidal shaped islands are cube-on-cube oriented, while those non-truncated shaped were mostly grown via rotational orientation. The island faceting could be explained by the surface energy anisotropy of both nickel and titanium nitride.

Magnetic characterization results show that both blocking temperature and coercivity of the ensemble of aligned nickel islands, which were grown in epitaxial titanium nitride matrix, are significantly higher than that of the ensemble of randomly oriented nickel islands, which were grown in polycrystalline/amorphous aluminum oxide matrix. These enhanced ferromagnetic properties are believed to comes from their self-assembled nature, which

alignes the magnetocrystlline anisotropy of the particles, and the self-organized nature, which enhances the particle interaction and leads to more symmetric reversal in a more coherent way.

Volmer-Weber growth by domain matching epitaxy is a very promising candidate for fabrication of self-assembled magnetic nanostructures.